NASA CR-159984

(NASA-CR-159984) GLOBAL EARTH RESPONSE TO LOADING BY OCEAN TIDE MODELS Final Report (Business and Technological Systems, Inc.) 64 p HC A04/MF A01 CSCL 08C

N80-24975

Unclas
G3/48 22281

June 1979

GLOBAL EARTH RESPONSE TO LOADING BY OCEAN TIDE MODELS

Ronald H. Estes

James M. Strayer

FINAL REPORT
Contract NAS 5-25010

submitted to

NASA
Goddard Space Flight Center
Greenbelt, Maryland 20771

by

BUSINESS AND TECHNOLOGICAL SYSTEMS, INC.
10210 Greenbelt Road
Seabrook, Maryland 20771

TABLE OF CONTENTS

1.0 INTRODUCTION

The ocean tides, with their principal semidiurnal and diurnal periods and their varying geometric patterns, act as sources for deforming the earth's crust and mantle. Understanding these deformations has importance for geodesy, geodynamics and oceanography. Moreover, information about the interior of the earth may be obtained through the magnitude and frequency dependence of the response of the solid earth to the tidal forces. The tide of the solid earth is composed of two basic responses; (1) a body tide due to the yielding of the earth to direct forces of the sun and moon and (2) a "load" tide produced by surface forces from the time varying ocean tides. It is difficult to distinguish between these two responses because their time dependence is similar, being driven by the same ultimate force. However, the nature of the driving force of the "body tide" is well understood, while the knowledge of the deep ocean tides through global numerical modeling is a recent advancement (Perkins and Accad (1969), Hendershott (1972), Zahel (1977), Estes (1977), Schwiderski (1978), Parke (1978)). The body tide varies in a relatively smooth nature over the earth's surface, depending principally on averaged overall elastic properties while the load tide is complicated by discontinuities of the surface load at coastal boundaries and by local ocean tide circulation (e.g. amphidromes and anti-amphidromes). Moreover, the displacement of the load tide is appreciable only in the crust and upper mantle, while the body tide has relatively large amplitude through most of the earth's interior. The load tide response then depends more on local crustal properties so that variations in near surface earth structure will be more reflected in the load tide.

The response of the solid earth to ocean loading may be evaluated by convolution of a model for the ocean tide over the global ocean with appropriate Green's functions which are derived from models of the earth's interior. In the present study, ocean tide models are used together with the Green's functions calculated by Farrell (1972)

in terms of a layered spherically symmetric Gutenberg-Bullen earth model to calculate global values of horizontal and vertical crustal displacement, gravity perturbation and strain at the earth's surface.

Recent global ocean tide models differ in detail and the accuracy with which the tides may be predicted from these models is uncertain. However, a measure of a model's overall accuracy may be provided by its agreement with recent astronomical calculations for the lunar acceleration and the rate of energy loss, which are simply related to the amplitude and phase of the (2,2) tesseral harmonic of the tidal elevation. Goad and Douglas (1977) have analyzed perturbations in satellite orbits which are also proportional to the low order harmonics and obtained values which show very close agreement with the astronomical values and the values calculated from the M_2 models of Schwiderski (1978) and Estes (1977). Although this provides some confidence in these two numerical M_2 models, it must be pointed out that close agreement with the (2,2) harmonic in a tidal model does not necessarily imply a correct model of the tides in specific regions. Tide solutions computed from Laplace's Tidal Equations fall into two groups; those constrained to agree with coastal observations and those which employ no data or constraints. The Estes (1977) tide models selected for the present study are of the second category and provide solutions for the M_2, S_2, N_2, K_2, K_1, O_1 and P_1 constituents integrated at 3° spacial resolution. The effects of ocean loading and self-gravitation have been included in deriving the M_2 model. These models are reasonable candidates for the global calculations of earth response for inland regions and open ocean areas, which are sensitive to the large scale effects of mid ocean tides. However, for coastal areas where the response is strongly influenced by local water tides, a model which provides a finer spacial resolution and incorporates coastal data constraints, such as a regional empirical model or the global Schwiderki (1978) model will provide greater accuracy to the convolution computation.

The results of the global calculations for crustal displacements, gravity anomalies and strains caused by ocean loading are presented in the form of corange and cotidal charts. The phases described by the cotidal contours are relative to the Greenwich meridian, and are expressed in hours instead of angular measurement. Hour values are obtained by dividing the phase expressed in degrees by 15 degrees per solar hour. In addition, a software package has been developed which will evaluate the vertical displacement due to loading by the principal tidal constituents and the solid earth tide as a function of geographic position and time as specified by user imput.

2.0 EARTH RESPONSE TO OCEAN LOADING

The calculation of the earth deformation due to surface mass loads closely follows the Green's function approach of Longman (1964) and Farrell (1972). Farrell has integrated the equations of motion for a self-gravitating elastic spherical earth using a Gutenberg-Bullen A earth model and produced load Love numbers h'_n, l'_n, and k'_n to high order n. The elastic earth response then reduces to a convolution of the ocean tide with the Green's function over the global ocean,

$$R(\phi,\lambda;t) = \iint R^2 \, \xi(\phi',\lambda';t) \, \rho G_f(\gamma) d\Omega' \tag{1}$$

where

$$\cos\gamma = \sin\phi\sin\phi' + \cos\phi\cos\phi'\cos(\lambda-\lambda')$$

and $\xi(\phi,\lambda;t)$ denotes the ocean tide and R is the mean radius of the earth. Here $G_f(\gamma)$ represents the point load Green's function transformed to an earth-fixed coordinate system and R represents the appropriate response. The total tide is approximated as a sum of constituent tides

$$\xi(\phi,\lambda;t) = \sum_i \xi_i \, (\phi,\lambda;t) \tag{2}$$

where

$$\xi_i(\phi,\lambda;t) = A_i(\phi,\lambda) \cos[\sigma_i(t-t_o)-\psi_i(\phi,\lambda)+\epsilon_i] \tag{3}$$

and constituents $i = \{M_2, S_2, N_2, K_2, K_1, O_1, P_1\}$ are available from global numerical models. Here t_o is January 0, 1900 and the phase function ψ is relative to the lunar passage at Greenwich of the

Table I

Constants for Constituent Tide Models

	M_2	S_2	N_2	K_2	K_1	O_1	P_1
Tidal Frequency, σ_i radians/sec	.1405189025 $x10^{-3}$	.1454441043 $x10^{-3}$	.137879702 $x10^{-3}$	.1458423167 $x10^{-3}$	.7292115836 $x10^{-4}$	.6759774403 $x10^{-4}$	.7252294561 $x10^{-4}$
Phase Constant, ϵ_i	18.5°	0.0°	82.4°	199.4°	189.69°	188.81°	170.29°

the ficticious moon for the particular constituent. The frequencies σ_i and constant phases ε_i are presented in Table I. The total response is then

$$R(\phi,\lambda;t) = \sum_i R_i(\phi,\lambda;t) \tag{4}$$

where

$$R_i(\phi,\lambda;t) = P_{i_{G_f}} cos[\sigma_i(t-t_o)+\varepsilon_i]+Q_{i_{G_f}} sin[\sigma_i(t-t_o)+\varepsilon_i] \tag{5}$$

and

$$\begin{aligned} P_{i_{G_f}}(\phi,\lambda) &\equiv \iint R^2\rho A_i(\phi',\lambda')cos[\psi_i(\phi',\lambda')]G_f(\gamma)sin\phi' d\phi' d\lambda' \\ Q_{i_{G_f}}(\phi,\lambda) &\equiv \iint R^2\rho A_i(\phi',\lambda')sin[\psi_i(\phi',\lambda')]G_f(\gamma)sin\phi' d\phi' d\lambda' \end{aligned} \tag{6}$$

In terms of amplitude A_i and phase Δ_i, the response to the i^{th} constituent is

$$R_i(\phi,\lambda;t) = A_i(\phi,\lambda)\, cos[\sigma_i(t-t_o) - \Delta_i + \varepsilon_i] \tag{7}$$

where

$$\begin{aligned} A_i(\phi,\lambda) &= \sqrt{P^2_{i_{G_f}} + Q^2_{i_{G_f}}} \\ \Delta_i(\phi,\lambda) &= tan^{-1}\left[\frac{Q_{i_{G_f}}}{P_{i_{G_f}}}\right] \end{aligned} \tag{8}$$

The appropriate Green's functions for the augmented potential and surface vertical and horizontal displacements at an angular distance γ (spherical earth) from a point load at the pole per unit of loading mass are

$$\phi'(\gamma) = \frac{Rg}{M_e} \sum_{n=0}^{\infty} k'_n P_n(\cos\gamma)$$

$$U'(\gamma) = \frac{R}{M_e} \sum_{n=0}^{\infty} h'_n P_n(\cos\gamma) \qquad (9)$$

$$V'(\gamma) = \frac{R}{M_e} \sum_{n=1}^{\infty} l'_n \frac{\partial P_n(\cos\lambda)}{\partial\gamma}$$

where M_e is the mass of the earth, R is the mean earth radius and g is the acceleration of gravity at the surface. Here primes on the Green's function denote that they are in a symmetric point load coordinate system. The Green's function for the differential gravity acceleration as given by Farrell (1972) is

$$G'(\gamma) = \frac{g}{M_e} \sum_{n=0}^{\infty} (n+2h'_n-(n+1)k'_n) P_n(\cos\gamma) \quad . \qquad (10)$$

Here $G'(\gamma)$ represents the difference between g, the acceleration of gravity at the earth's surface, and the acceleration on the deformed surface after application of the ocean load. Following Farrell, we break the acceleration Green's function into direct, or Newtonian acceleration

$$G'^{N}(\gamma) = \frac{g}{M_e} \sum_{n=0}^{\infty} n P_n(\cos\gamma) \qquad (11)$$

and elastic acceleration

$$G'^{E}(\gamma) = G'(\gamma) - G'^{N}(\gamma)$$

$$= \frac{g}{M_e} \sum_{n=0}^{\infty} [2h_n' - (n+1)k_n'] P_n(\cos\gamma) \quad . \tag{12}$$

As pointed out by Pekeris (1978), equation (10) applies to gravity measurements made at a point below the tidal loading sheet. For points above the sea, the increase in gravity caused by crossing the loading sheet from below

$$-4\pi G \rho \xi \tag{13}$$

must be added to equation (10) which results in

$$G'(\gamma) = \frac{g}{M_e} \sum_{n=0}^{\infty} [2h_n' - (n+1)(1+k_n')] \quad . \tag{14}$$

The correction term of equation (13) may be written

$$- \frac{3\rho}{\bar{\rho}} g \frac{\xi}{R} \tag{15}$$

where ρ denotes the density of sea water and $\bar{\rho}$ the mean density of the earth. For gravity measurements on the coast this correction is important. However, for inland measurements where there is no ocean tide the correction term is zero. Pekeris (1978) also points out that in evaluating the Newtonian acceleration Green's function of equation (11), Ferrell (1972) has omitted the delta function from the expression

$$\sum_{n=0}^{\infty} n P_n(x) = - \frac{1}{2\sqrt{2-2x}} + \delta(1-x)$$

and thus a term

$$\frac{3}{2}\frac{\rho}{\bar{\rho}}\cdot\frac{S}{R}\frac{\xi}{R} \tag{16}$$

should be added to the gravity perturbation. Again, this term contributes only over ocean areas. Similarly, expressions may be obtained for the Green's functions of the non-zero elements of the strain tensor at the earth's surface. As pointed out by Farrell (1972), these Green's functions are slowly convergent series and must be summed to large values of n .

The summed values for the Green's functions as a function of angle have been taken from tables given by Farrell (1972), where values are available for U', V', G' and $S'_{\gamma\gamma}$, and S' is the strain tensor. The other diagonal components of the strain tensor (off-diagonals are zero for the symmetric point load coordinate system, with load at the pole, for which the Green's functions are derived) are calculated from

$$\begin{aligned} S'_{\gamma\gamma} &= \frac{U'}{a} + \cot\theta\,\frac{V'}{a} \\ S'_{rr} &= -\frac{\lambda(a)}{\sigma(a)}\,(S_{\gamma\gamma}+S_{\lambda\lambda}) \end{aligned} \tag{17}$$

where $\lambda(a)$ and $\sigma(a)$ are the Lamé parameters at the top layer of the earth model. Here γ is colatitude and λ longitude in the symmetric point load coordinates. To evaluate the convolutions for the earth response of equation (1), it must be realized that the primed Green's functions described above are with respect to the symmetric point load coordinate system, and to resolve components of vector and tensor quantities appropriate transformations must be applied. Let (ϕ,λ) be the latitude and longitude of the point of evaluation for the convolution and (ϕ',λ') be the latitude and

longitude of the water column being considered as the load. Moreover, let $\hat{r}$, $\hat{\theta}$, $\hat{\lambda}$ denote the unit vectors in the direction of increasing r, θ, λ at the point of evaluation (where θ is the co-latitude). Then the Green's functions for the horizontal displacement in the $\hat{\theta}$ and $\hat{\lambda}$ directions, respectively, are

$$V_\theta(\gamma) = V'(\gamma)\cos\alpha$$
$$V_\lambda(\gamma) = V'(\gamma)\sin\alpha \qquad (18)$$

where

$$\cos\alpha = \frac{\sin\phi' - \sin\phi\cos\gamma}{\cos\phi\sin\gamma} \qquad (19)$$
$$\sin\alpha = \frac{\cos\phi'\sin(\lambda-\lambda')}{\sin\gamma}$$

and as before

$$\cos\gamma = \sin\phi\sin\phi' + \cos\phi\cos\phi'\cos(\lambda-\lambda') \qquad (20)$$
$$\sin\gamma = \sqrt{1-\cos^2\gamma} \quad .$$

Similar expressions for the radial displacement and strain tensor components are

$$
\begin{aligned}
U(\gamma) &= U'(\gamma) \\
S_{rr} &= S'_{rr} \\
S_{\theta\theta} &= \cos^2\alpha\, S'_{\gamma\gamma} + \sin^2\alpha\, S'_{\lambda\lambda} \\
S_{\lambda\theta} &= \sin\alpha\cos\alpha\, (S'_{\gamma\gamma} - S'_{\lambda\lambda}) \\
S_{\lambda\lambda} &= \sin^2\alpha\, S'_{\gamma\gamma} + \cos^2\alpha\, S'_{\lambda\lambda} \quad .
\end{aligned}
\tag{21}
$$

The computation for the response convolutions of equation (1) is performed at each 3°x3° equal-angular grid point over the surface of the globe using the Estes (1977) 3° resolution models. Cotidal and corange charts for the principal constituents are presented in Figures 1-7. Numerically, the quadrature is evaluated as the sum of near zone and far zone contributions. The far zone is defined as the collective region of 3°x3° surface areas whose centers are greater than 3° from the point of evaluation. Since the tide models define values only at equal-angular 3°x3° grid points, the tide amplitude and phase are considered constant within each 3°x3° surface area element. The far zone contributions to equation (1) are then obtained by summing the individual area elements with the Green's function evaluated at the central angle between the center of the element and the point of evaluation. In the near zone, the Green's functions change so rapidly that the elements of surface area are evaluated on a graduated scale from $\frac{1}{100}° \times \frac{1}{100}°$ to $\frac{1}{10}° \times \frac{1}{10}°$ as the integration proceeds away from the point of evaluation. Again, the tide amplitude and phase are considered constant within each 3°x3° surface area.

The computation for the earth response is greatly influenced by the near zone contribution in most ocean and coastal areas. In the open ocean areas the Estes (1977) tide models and the assumption of

constant tidal amplitude and phase within a 3°x3° surface area are adequate. However, near coastal zones the calculations suffer from the fact that the global numerical tide models used are theoretical solutions of the Laplace Tidal Equations for the open ocean areas of depths greater than approximately 500 meters and the solutions contain no data. Moreover, the 3° approximation to coastline geometry is course. Accurate near zone values for coastal regions should be obtained from more detailed regional tide models or from finer spacial resolution global models, such as the M_2 model developed by Schwiderski (1978), that have incorporated coastal tide observations into the solution to more precisely represent the real near shore variation. Because of these considerations, the calculations presented in this study for regions within 1° to 3° of coastlines should be viewed qualitatively in the transition from open ocean to inland areas. Note also that the tide models used in the calculations predict only to 81° north latitude, and the tide is assumed to be zero above this limit. The responses evaluated in the north polar regions then are only the far zone contributions. Near zone contributions should be computed from a special pole tide model.

2.1 Crustal Displacements

The vertical response due to ocean loading by constituent "i" as given by equation (7) is

$$U_i(\phi,\lambda;t) = A_u(\phi,\lambda)\cos[\sigma_i(t-t_o) + \varepsilon_i - \Delta_i(\phi,\lambda)]$$

where the amplitudes and phases are calculated by convolution with the Green's function from equation (9)

$$G_f(\gamma) \equiv U'(\gamma) \quad .$$

Corange and cotidal maps for constituents M_2, S_2, N_2, K_2, K_1, O_1 and P_1 are presented in Figures 8 through 14. As indicated previously, the phases are with respect to lunar passage of Greenwich. Horizontal responses

$$V_{\theta_j}(\phi,\lambda;t)$$

$$V_{\lambda_j}(\phi,\lambda;t)$$

calculated from the Green's functions of equation (18) were evaluated only for the M_2 tide and are presented in Figures 15 and 16.

The vertical response exhibits a spacial behavior over the oceans which resembles the structure of the constituent tidal heights. The greatest amplitudes are on the order of 5 cm. in the region of the mid-Pacific anti-amphidrome predicted by the M_2 model, while over continental areas the calculated load response is generally less than 1 cm. and decreases with distance from the coasts. Horizontal displacements are an order of magnitude smaller than the vertical displacements and exhibit a more complex structure.

2.2 Gravity Perturbations

The measurement of gravitational acceleration is the resultant of components

$$g = g_1 + g_2 + g_3 + g_4 \qquad (22)$$

where g_1 represents the acceleration on a rigid earth, g_2 represents the contribution from a symmetric, oceanless, elastic earth, g_3 represents the contribution from ocean tides, and g_4 is the response of regional anomalous geologic structure. The components g_1 and g_2 are the larger terms and have essentially the same phase, while the terms g_3 and g_4 may differ considerably from other terms with respect to phase.

Modern gravimeters are capable of detecting the g_3 and g_4 contributions with limited precision, and it is now clearly established that earth tidal gravity parameters for both coastal and inland measurements are sensitive to the regional and global ocean tides. A

comparison of accurately measured patterns of tidal gravity spacial variation within continental regions with model calculations will offer the ability to distinguish between tide models and establish their levels of precision. In fact, Kuo, et al. (1970) attempt to indirectly map the ocean tides by solving the inverse problem of the response of tidal gravity to ocean tide loading. The accuracy of data will be greatly improved with the use of a new type of superconducting gravimeter (Warburton, et al (1975)). Presently measurements using this instrument are available only at La Jolla and Piñon Flat, California.

Calculations of tidal gravity at specified stations using available tide models and the comparison of results with observations have been performed by several authors. In particular, Robinson (1974) compared the observed relative gravimetric factors of M_2 and O_1 at several stations in the southeastern United States using five different published global M_2 models. Wilson (1978) has extended the analysis using additional ocean tide models and a model for the Gulf of Mexico. Bretreger and Mather (1978) have analysed tidal gravity measurements in Australia using a ten-parameter response model and global M_2 tide models. However, only Kagan and Polyakov (1977) using an M_2 model by Gordeyev, et al (1976) have performed calculations over the entire earth to present a global picture of variation.

The amplitude of the gravimetric factor

$$\delta = 1 - \frac{3}{2} k + h$$

where k and h are Love numbers, is the ratio of tidal gravity at a point on the earth to the theoretical amplitude on a rigid earth. The local epoch of a measurement is the phase difference between the observed gravity and theoretical gravity. In the absence of ocean loading the value of the gravimetric factor would be approximatly 1.16. The correction $\Delta\delta$ is defined by vectorial addition of the ocean load gravity vector to the theoretical gravity

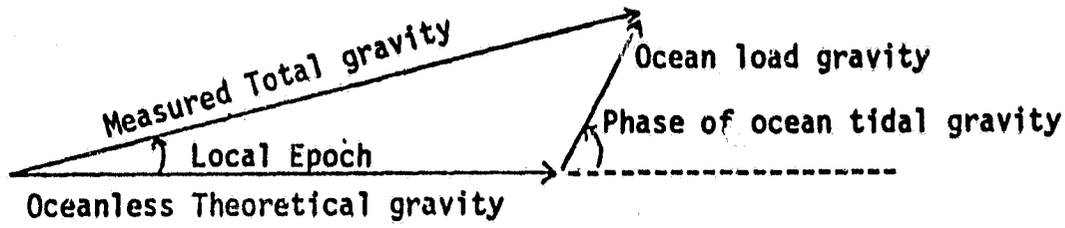

where the g_4 contribution is assumed negligible for gravity and the theoretical gravity has zero phase lag. Note that the phase of the ocean tidal gravity in this diagram is with respect to the phase of the theoretical gravity. The relation between the local phase of theoretical gravity and the Greenwich phase is

$$\text{Local Phase} = \text{Greenwich Phase} + m\lambda$$

where λ is the east longitude of the measurement point and m is the order of the tide (2 for semidiurnal and 1 for diurnal tides). The amplitude of the ocean load gravity in μgal is obtained from the amplitude $|\Delta\delta|$ multiplied by the amplitude of the theoretical gravity of the rigid earth.

The ocean loading gravity perturbations for the M_2 and O_1 tides are calculated from the Green's function of equations (11) and (12) for the Newtonian and elastic contributions and are presented in figures 17 through 20. Here the calculation for the Newtonian term neglects the delta function pointed out by Pekeris (1978). For coastal and ocean areas the additional term given by equation (16) may be evaluated from the ocean tide maps given in Figures 1 through 7. Moreover, for measurements evaluated at coastal and ocean points above the tide sheet, the correction term given by equation (15) must be added to obtain the total gravity perturbations. The amplitude and phases of the gravity perturbations, as with the horizontal crustal deviations, exhibits a spacial behavior which resembles the tide structure. This supports the suggestion that the complexity of the ocean tidal gravity is due to the complexity of the global tide rather than the response of the earth to the ocean tidal loading.

The responses are on the order of one μgal over continental regions and decrease with distance from the coasts. Values measured by Warburton, et. al. (1975) at Piñon Flat for the O_1 and M_2 tidal gravity components using the superconducting gravimeter are in reasonable agreement with the calculations presented in Figures 17 through 20. However, their measurements on the coast at La Jolla (on the order of 100 km. distance from Piñon Flat) are substantially greater than the results shown in Figures 17 through 20. This is most likely a consequence of the inadequate precision in modeling the near zone ocean tide at the coasts as discussed in Section 2.0.

2.3 Strains

A comparison of precise tidal strain observations with model predictions could provide insight into the nature of the earth and its structure. However, obtaining accurate measurements of tidal strains is considerably more complicated than for tidal gravity. While g_4 from equation (22) is considered negligible for tidal gravity, tidal strain measurements are very sensitive to local topographic and geologic anomolous influences. A basic understanding of the ocean tidal loading strains and the local influences could have a great impact on the field of techtonic geophysics. In particular, Young and Zürn (1979) claim to have provided weak evidence that earthquakes in the Swabian Jura are triggered by tidal shear stress. The concept that ocean load tide strains could provide a mechanism for triggering is feasible, as ocean loading can introduce appreciable horizontal shear strains when loading is not laterally uniform, such as near a coastline.

The ocean loading tidal strain tensor have been evaluated for the M_2 tide from convolution with the strain component Green's functions of equation (21). The symmetric tensor is written

$$S = \begin{pmatrix} e_{\gamma\gamma} & 0 & 0 \\ 0 & e_{\theta\theta} & e_{\theta\lambda} \\ 0 & e_{\lambda\theta} & e_{\lambda\lambda} \end{pmatrix} \qquad (23)$$

where each element varies with time as

$$e_{ij}(\phi,\lambda;t) = A_{\varepsilon_{ij}}(\phi,\lambda)\cos[\sigma_{M_2}(t-t_o)-\Delta_{\varepsilon_{ij}}(\phi,\lambda)+\varepsilon_{M_2}] \quad .$$

Note that the tensor has only three independent components at the free earth surface, since

$$e_{rr} = -\frac{\lambda(a)}{\sigma(a)}(e_{\theta\theta}+e_{\lambda\lambda}) \quad .$$

where $\lambda(a)$ and $\sigma(a)$ are Lamé parameters at earth radius, a. The horizontal surface strain tensor may be written in the form

$$\begin{pmatrix} e_{\theta\theta} & e_{\theta\lambda} \\ e_{\lambda\theta} & e_{\lambda\lambda} \end{pmatrix} = \begin{pmatrix} \frac{1}{2}(e_{\theta\theta}+e_{\lambda\lambda}) & 0 \\ 0 & \frac{1}{2}(e_{\theta\theta}+e_{\lambda\lambda}) \end{pmatrix}$$

$$+ \begin{pmatrix} \frac{1}{2}(e_{\theta\theta}-e_{\lambda\lambda}) & e_{\theta\lambda} \\ e_{\theta\lambda} & -\frac{1}{2}(e_{\theta\theta}-e_{\lambda\lambda}) \end{pmatrix} \qquad (24)$$

$$= -\frac{\sigma(a)}{2\lambda(a)} e_{rr}\, I + \begin{pmatrix} \frac{1}{2}(e_{\theta\theta}-e_{\lambda\lambda}) & e_{\theta\lambda} \\ e_{\theta\lambda} & -\frac{1}{2}(e_{\theta\theta}-e_{\lambda\lambda}) \end{pmatrix}$$

as the sum of a pure areal strain and a pure shear strain. While it is conventional to represent the three independent components of the surface strain tensor by plotting the linear strain at a particular geographic position as a function of azimuth on a polar diagram, we present more detailed corange and cotidal plots of the elements e_{rr}, $e_{\theta\theta}$, $e_{\lambda\theta}$ and $e_{\lambda\lambda}$ in Figures 21 through 28. Due to plotting difficulties the tensor components are presented in separate figures over ocean areas and land areas.

The radial strain component shown in Figures 21 indicates strains of the order of 5×10^{-10} in the mid-oceans and 1×10^{-10} over continents. The transitions over coastal areas appear generally smooth. This is in contrast to the $e_{\theta\theta}$ and $e_{\lambda\lambda}$ components of Figures 22 through 25. Here the mid-ocean strains are on the order of 5×10^{-8} while strains over continental regions are two orders of magnitude smaller. The steep gradients occur at the shorelines, where abrupt changes in phase are also observed. Note that the amplitudes of $e_{\theta\theta}$ and $e_{\lambda\lambda}$ are nearly equal while their phases are nearly 180° apart. This is consistent with e_{rr}, which is proportional to their sum, being two orders of magnitude smaller. The $e_{\lambda\theta}$ strains of Figures 26 and 27 show a comparable magnitude to $e_{\theta\theta}$ and $e_{\lambda\lambda}$ over continental areas, while being approximately an order of magnitude smaller over mid oceans. Figure 28 displays that the $e_{\lambda\theta}$ strain generally shows a sharp increase in magnitude to the order of 5×10^{-8} near coastlines before rapidly falling to smaller values over land areas. Abrupt changes in phase also occur near shorelines. By equation (24), these values show that the ocean load strains are dominated by pure shear, while the areal strains are small.

3.0 COMPUTER SOFTWARE FOR BODY AND LOAD TIDE RADIAL DISPLACEMENT

A computer program has been developed to evaluate the radial displacements given in Section 2.1 due to ocean loading and the total radial displacement due to the solid earth tides (body tides) at a user specified position on the earth for a desired time interval. The algorithm evaluates the contributions from the ocean tidal constituents and the body tide individually for a one day period at one hour increments. Required input are the Modified Julian Day and the geodetic coordinates of the point of interest.

The radial ocean loading displacements of Section 2.1 are represented in the software in the form of spherical harmonic expansions

$$\begin{aligned} U_i(\phi,\lambda;t) &= A_u(\phi,\lambda)\, cos[\sigma_i(t-t_o)+\varepsilon_i-\Delta_i(\phi,\lambda)] \\ &= \{\sum_{n,m} [a_{nm} cos m\lambda + b_{nm} sin m\lambda] P_{nm}(sin\phi)\} cos(\sigma_i(t-t_o)+\varepsilon_i) \\ &+ \{\sum_{n,m} [c_{nm} cos m\lambda + d_{nm} sin m\lambda] P_{nm}(sin\phi)\} sin(\sigma_i(t-t_o)+\varepsilon_i) \end{aligned} \tag{25}$$

where the coefficients a_{nm}, b_{nm}, c_{nm} and d_{nm} are obtained by a least squares fit to degree and order twelve. These expansions provide an accurate and compact method for evaluating the ocean loading tides. The body tide elevation is given by

$$U_B(\phi,\lambda;t) = \frac{M_d R_e}{M_e} \sum_{n=2}^{\infty} h_n \left(\frac{R_e}{R_d}\right)^{n+1} P_n(cos\Theta_{MS}) \tag{26}$$

where M_d is the mass of the disturbing body (Moon or Sun), R_d is the geocentric distance to the body and h_n are Love numbers. The angle Θ_{MS} denotes the geocentric zenith angle of the moon (sun) from the point of elevation. The terms in the expansion fall off rapidly so only the first term

is of major significance. The radial body tide, U_B, is then evaluated as

$$U_B \ (\phi,\lambda;t) = \frac{M_d}{M_e}\left(\frac{R_e}{R_d}\right)^3 \frac{R_e h_2}{2}\left[3(\hat{R}_d\cdot\hat{r})^2-1\right] \qquad (27)$$

where $\hat{r}$ represents the unit radius vector at the point of interest on the earth:

$$\hat{r} = [cos\phi cos\lambda,\ cos\phi sin\lambda,\ sin\phi]$$

where geodetic latitude, ϕ, and longitude, λ, are program inputs.

$\hat{R}_d$ represents the unit vector from the center of the earth in the direction of the disturbing body:

$$\hat{R}_d = [\lambda',\mu',\nu']$$

where λ', μ', ν' give the position in earth-fixed coordinates.

In calculating $\hat{R}$ for the moon, a true longitude and the latitude (above the plane of the ecliptic) are derived from the Hill-Brown theory using the Modified Julian Day. Brown's tables express the coordinates of the moon as sums of periodic terms whose arguments are algebraic sums of the multiples of ℓ, ℓ', F, D, r. See Tables II and III.

TABLE II
Ecliptic Elements

MJD = Modified Julian Day

$D = MJD - 2415020.0$

$D1 = D * 1.E-4$

$\ell = 296.104608 + 13.0649924465 * D + 0.0006889 * (D1)^2$

$\ell' = 358.475845 + 0.9856002670 * D - 0.0000112 * (D1)^2$

$F = 11.250889 + 13.2293504490 * D - 0.0002407 * (D1)^2$

$D = 350.737486 + 12.1907491914 * D - 0.0001076 * (D1)^2$

$\Gamma = 281.220833 + 0.470684 * D1 + 0.339E-4 * (D1)^2$

$\varepsilon = 23.452294 - 0.0035626 * D1 - 0.123E-6 * (D1)^2$

$\theta_g = 99.6904833 + 360.98564733 * D - 180.0$

Table III Development of Lunar Position

Coeff of sine in $\delta\lambda_m$. (Seconds of arc)	Multiples of ℓ	ℓ'	F	D	r
22639.5	1	0	0	0	0
-4586.426	1	0	0	-2.	0
2369.902	0	0	0	2	0
769.016	2	0	0	0	0
-668.111	0	1	0	0	0
-411.608	0	0	2	0	0
-211.656	2	0	0	-2	0
-205.962	1	1	0	-2	0
-125.154	0	0	0	1	0
191.953	1	0	0	2	0
-165.145	0	1	0	-2	0
147.693	1	1	0	0	0
-109.667	1	1	0	0	0
Coeff in sine in Latitude, ϕ_m (Seconds of arc)					
18461.48	0	0	1	0	0
1010.180	1	0	1	0	0
-999.695	-1	0	1	0	0
-623.658	0	0	1	-2	0
117.262	0	0	1	2	0
199.485	-1	0	1	2	0
-166.577	1	0	1	-2	0
61.913	2	0	1	0	0

Table IV Development of $\sin \lambda_s$ and $\cos \lambda_s$

Coef. × 10^5 of cosine in $\cos \lambda_s$ and of sine in $\sin \lambda_s$	Multiples of ℓ	ℓ'	F	D	r
99972	0	1	0	0	1
1674	0	2	0	0	1
32	0	3	0	0	1
1	0	4	0	0	1
2	0	1	0	1	1
-1675	0	0	0	0	1
-4	0	-1	0	0	1
-2	0	1	0	-1	1
4	0	0	1	-1	0
-4	0	2	-1	1	2

The derived ecliptic lunar position (ϕ_m, λ_m) is converted to inertial coordinates

$$\lambda' = \cos\lambda_m \cos\phi_m$$

$$\mu' = \sin\lambda_m \cos\phi_m \cos\varepsilon - \sin\phi_m \sin\varepsilon$$

$$\nu' = \sin\phi_m \cos\varepsilon + \sin\lambda_m \cos\phi_m \sin\varepsilon$$

where ε is the obliquity to the ecliptic and

$$\lambda_m = \ell' + D + \Gamma + \delta\lambda_m \quad .$$

The conversion to earth-fixed coordinates is accomplished by a matrix transformation

$$\left(\hat{R}_d\right)_{EF} = \left(M\hat{R}_d\right)_{\text{Inertial}} \tag{28}$$

where

$$M = \begin{pmatrix} \cos\Theta_g & \sin\Theta_g & 0 \\ -\sin\Theta_g & \cos\Theta_g & 0 \\ 0 & 0 & 1 \end{pmatrix}$$

and Θ_g is the Greenwich hour angle (Table II).

The unit vector $\hat{R}_d$ in the direction of the sun is derived from Newcomb's theory in the same manner. The ecliptic elements, ℓ, ℓ', F, D, Γ, are the same as for the lunar development. The solar coordinates $(\cos\lambda_s, \sin\lambda_s)$ are expressed as algebraic sums as listed in Table IV

The conversion to equatorial coordinates is

$$\lambda' = \cos\lambda_s$$

$$\mu' = \sin\lambda_s \cos\varepsilon$$

$$\nu' = \sin\lambda_s \sin\varepsilon$$

and a final transformation to earth-fixed coordinates is applied, using Equation (28).

A comparison of the radial body tide displacement computed by this analytic procedure and the ephemeris calculation from GEODYN is displayed in Figure 20.

4.0 NEW TECHNOLOGY

The effort under this contract consisted of the development and programming of techniques to numerically calculate earth response to global semidiurnal and diurnal ocean tide models. Global Vertical crustal deformations have been evaluated for M_2, S_2, N_2, K_2, K_1, O_1, and P_1 ocean tide loading, while horizontal deformations have been evaluated for the M_2 tidal load. Tidal gravity calculations were performed for M_2 and O_1 tidal loads, and strain tensor elements were evaluated for M_2 loads. The M_2 solution used for the ocean tide included the effects of self-gravitation and crustal loading.

Frequent reviews and a final survey for new technology were performed. It is believed that the mathematical and programming techniques and algorithms developed do not represent "reportable items," or patentable items, within the meaning of the New Technology Clause. Our reviews and final survey found no other items which could be considered reportable items under the New Technology Clause.

5.0 REFERENCES

1. Bretreger, k. and R. S. Mather, 1978. Modelling Ocean-Loading Effects on Tidal Gravity in Australia, Geophys. J. R. Astr. Soc., 52, 241-257.
2. Cartwright, D. E., 1977. Oceanic Tides, Rep. Prog. Phys., 40, 665-708.
3. Estes, R. H., 1977. A Computer Software System for the Generation of Global Ocean Tides Including Self-Gravitation and Crustal Loading Effects, X-920-77-9, Goddard Space Flight Center.
4. Farrell, W. E., 1972. Deformation of the Earth by Surface Loads, Revs. of Geophys. and Space Phys., 10, 761-797.
5. Felsentreger, T.L., Marsh, J.G. and R. G. Williamson, 1978. M_2 Ocean Tide Parameters and the Deceleration of the Moon's Mean Longitude from Satellite Orbit Data, NASA TM-79571, Goddard Space Flight Center, Greenbelt, Maryland.
6. Goad, Clyde C., 1977. Application of Digital Filtering to Satellite Geodesy, NOAA T.R. NOS 71 NGS 6, U.S. Dept. of Commerce, National Oceanic and Atmospheric Administration, National Ocean Survey.
7. Goad, Clyde C. and Bruce C. Douglas, 1977. Lunar Longitude Deceleration and Tidal Parameters Estimated from Satellite Orbital Perturbations, Eighth International Symposium on Earth Tides, Bonn, Federal Republic of Germany, September 19-24, 1977.
8. Hendershott, M. C., 1972. The Effects of Solid Earth Deformation on Global Ocean Tides, Geophys. J. R. Astr. Soc., 29, 389-402.
9. Kagan, B.A. and Y.V. Polyakov, 1977. The Effect of Ocean Tides on the Tidal Variations of Gravity, Oceanology, Vol. 17, No. 6.
10. Klein, F. W., 1976. Earthquake swarms and the Semidiurnal Solid Earth Tide, Geophys. J., 45, 245-295.
11. Kuo, J. T., 1975. Earth Tides, Rev. Geophys. and Space Physics, Vol. 13, No. 3.
12. Kuo, J. T., R. C. Jachens, M. Ewing and G. White, 1970. Transcontinental Tidal Gravity Profile Across the United States, Science, 168, pg. 968-971.

13. Longman, I. M., 1963. A Green's Function for Determination of the Deformation of the Earth Under Surface Mass Loads, 2. Computations and Numerical Results. J. Geophysical Research, 68, pg. 485-496.
14. Parke, M.E., 1978. Global Modeling of Tides on an Elastic Earth, Symposium on Long Waves in the Ocean, Ottawa, June 6-8, 1978. Published in Manuscript Report Series No. 53, 1979, Department of Fisheries and the Environment, Marine Sciences Directorate, Ottawa, Canada.
15. Pekeris, C. L., 1978. The Bodily Tide and the Yielding of the Earth Due to the Tidal Loading, Geophys., J. R. Astronomical Society, 52, 471-478.
16. Pekeris, C. L. and Y. Accad, 1969. Solution of Laplaces' Equations for the M_2 Tide in the World Oceans, Phil. Trans. Royal Soc. London, A., 265, pg. 413-436.
17. Schwiderski, E. W., 1978. Global Ocean Tides, Part I: A Detailed Hydrodynamical Interpolation Model, NSWC/DL TR-3866, Naval Surface Weapons Center, Dahlgren Laboratory, Dahlgren, Va.
18. Slichter, L. B., 1970. Earth Tides, in the Nature of the Solid Earth, E. C. Robertson, editor, McGraw-Hill, 1972. Paper presented at a symposium held at Harvard University, Cambridge, Massachusetts, April 16-18, 1970.
19. Warburton, R. J., Beaumont, C., and J. M. Goodkind, 1975. The Effect of Ocean Tide Loading on Tides of the Solid Earth Observed with the Superconducting Gravimeter," Geophys, J.R. Astr. Soc., 43, 707-720.
20. Warburton, R. J. and J. M. Goodkind, 1978. Detailed Gravity-Tide Spectrum Between One and Four Cycles Per Day, Geophysical Journal of the Royal Astronomical Society, 52, 117-136.
21. Wilson, Deborah C., 1978. Ocean Tidal Loading in Southeastern United States, M.S. Thesis. NOAA Grant No. 04-7-150-44116, Department of Geological Sciences, Virginia Polytechnic Institute and State University.
22. Young, D. and W. Zurn, 1979. Tidal Triggering of Earthquakes in the Swabian Jura, J. Geophys., 45, 171-182.
23. Zahel, W., 1977. A Global Hydrodynamic-Numerical 1° Model of the Ocean Tides; the Oscillation System of the M_2-Tide and its Distribution of Energy Dissipation, Ann. Geophys, 33, 31-40.

FIGURE 1 : Converged M_2 Tide Model including ocean loading and self-gravitation effects integrated on a 3°x3° global grid.

ϕ: Dashed lines --- cotidal lines (phase) in hours

A: Solid lines —— corange lines (amplitude) in centimeters

$\xi(\phi,\lambda;t) = A(\phi,\lambda)\ cos[\sigma t-\psi]$

σ = .00014052 radians/sec

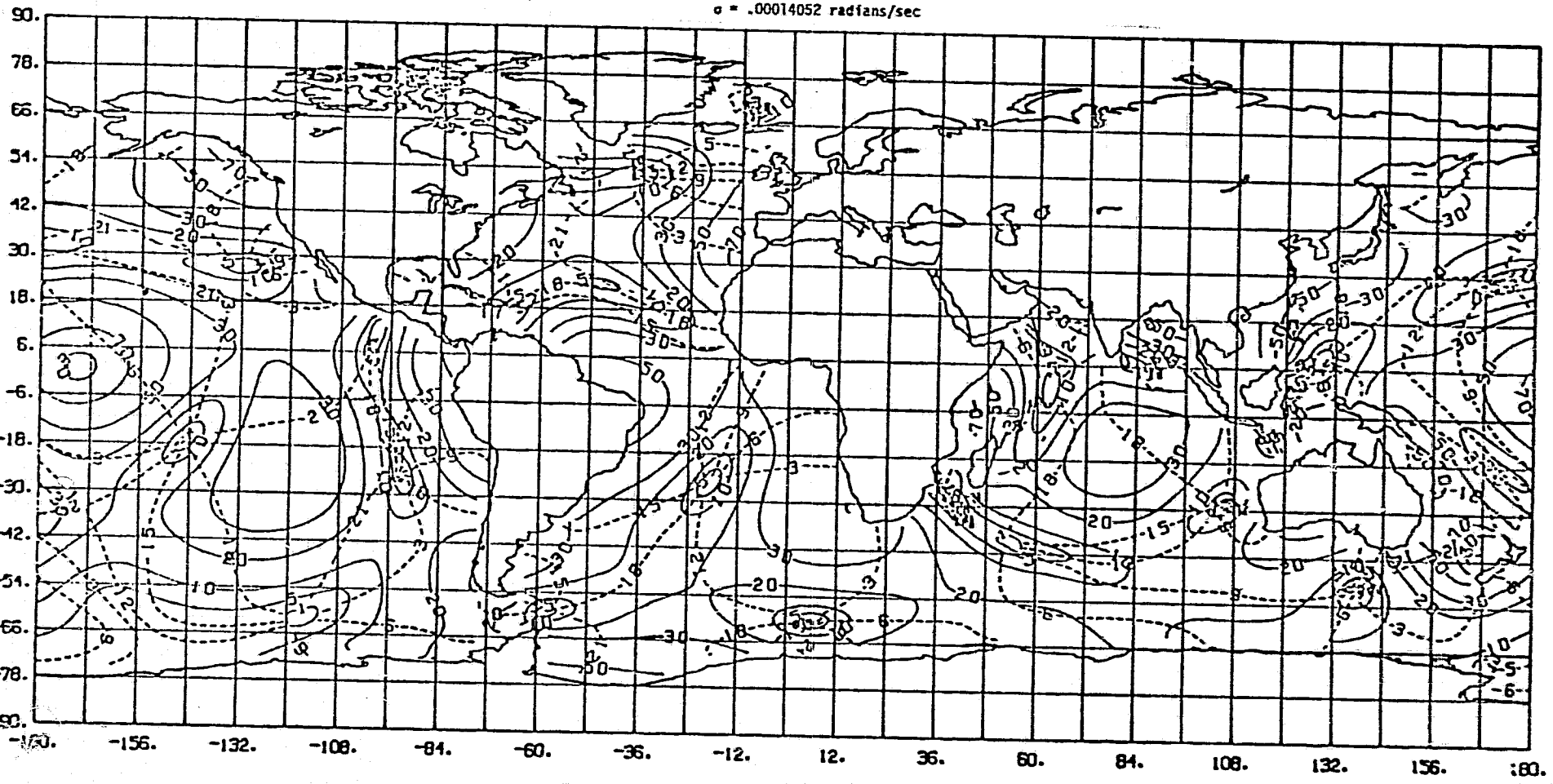

FIGURE 2: S_2 Tide Model neglecting ocean loading and self-gravitation effects integrated on a 3°x3° global grid.

ψ: Dashed lines --- cotidal lines (phase) in hours

A: Solid lines —— corange lines (amplitude) in centimeters

$\xi(\phi,\lambda;t) = A(\phi,\lambda)\ cos[\sigma t - \psi]$

σ = .0001454452 radians/sec

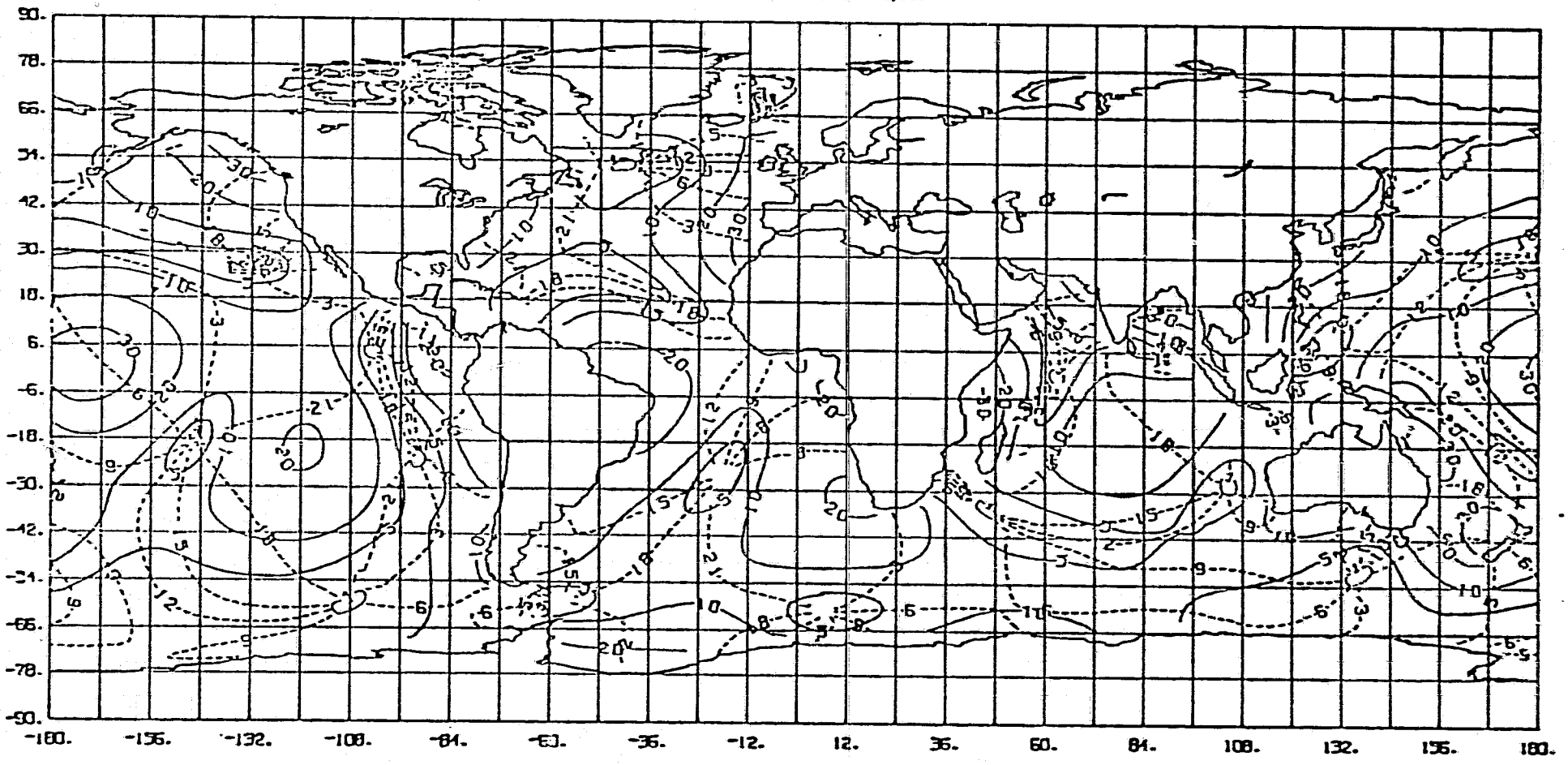

FIGURE 3: M_2 Tide Model neglecting ocean loading and self-gravitation effects integrated on a 3°x3° global grid.

ϕ: Dashed lines --- cotidal lines (phase) in hours

A: Solid lines —— corange lines (amplitude) in centimeters

$\zeta(\phi,\lambda;t) = A(\phi,\lambda)\ cos[\sigma t-\phi]$

σ = .00013788 radians/sec

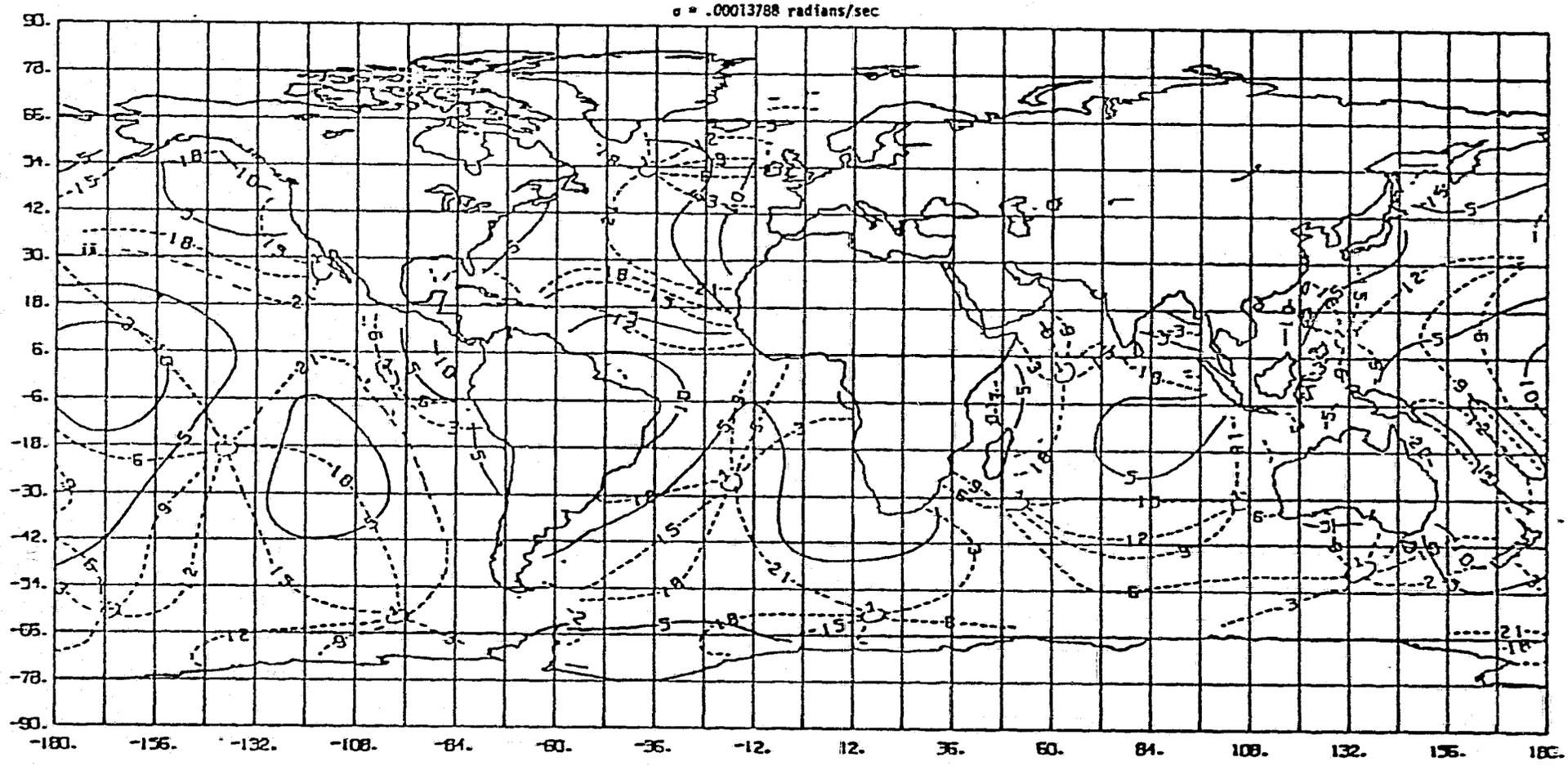

FIGURE 4: K_2 Tide Model neglecting ocean loading and self-gravitation effects integrated on a 3°x3° global grid.

ψ: Dashed lines --- cotidal lines (phase) in hours

A: Solid lines —— corange lines (amplitude) in centimeters

$\zeta(\phi,\lambda;t) = A(\phi,\lambda)\cos[\sigma t-\psi]$

σ = .00014584 radians/sec

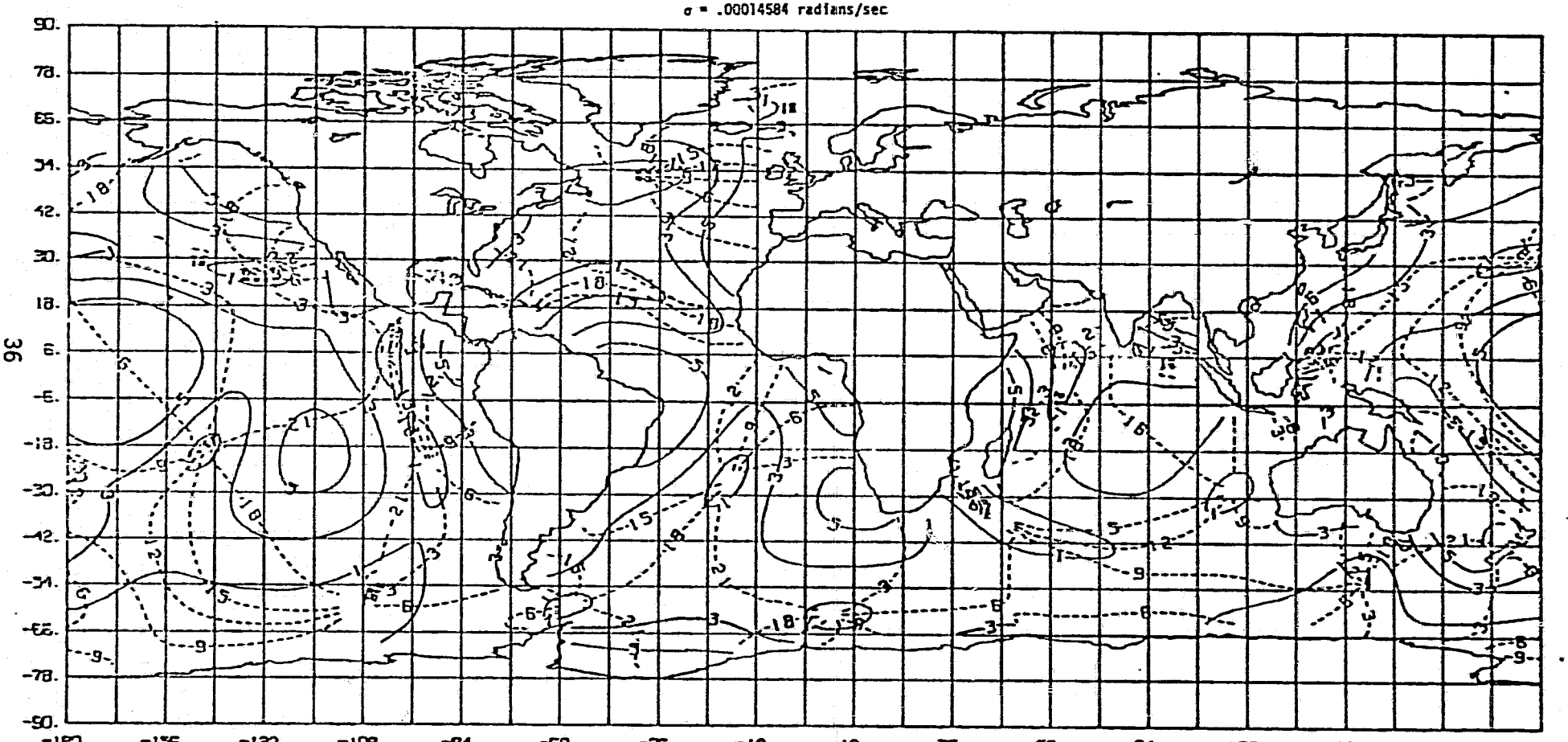

FIGURE 5: K_1 Tide Model neglecting ocean loading and self-gravitation effects integrated on a 3°x3° global grid.

ϕ: Dashed lines --- cotidal lines (phase) in hours

A: Solid lines —— corange lines (amplitude) in centimeters

$\zeta(\phi,\lambda;t) = A(\phi,\lambda)\ cos[\sigma t - \phi]$

σ = .0000729216 radians/sec

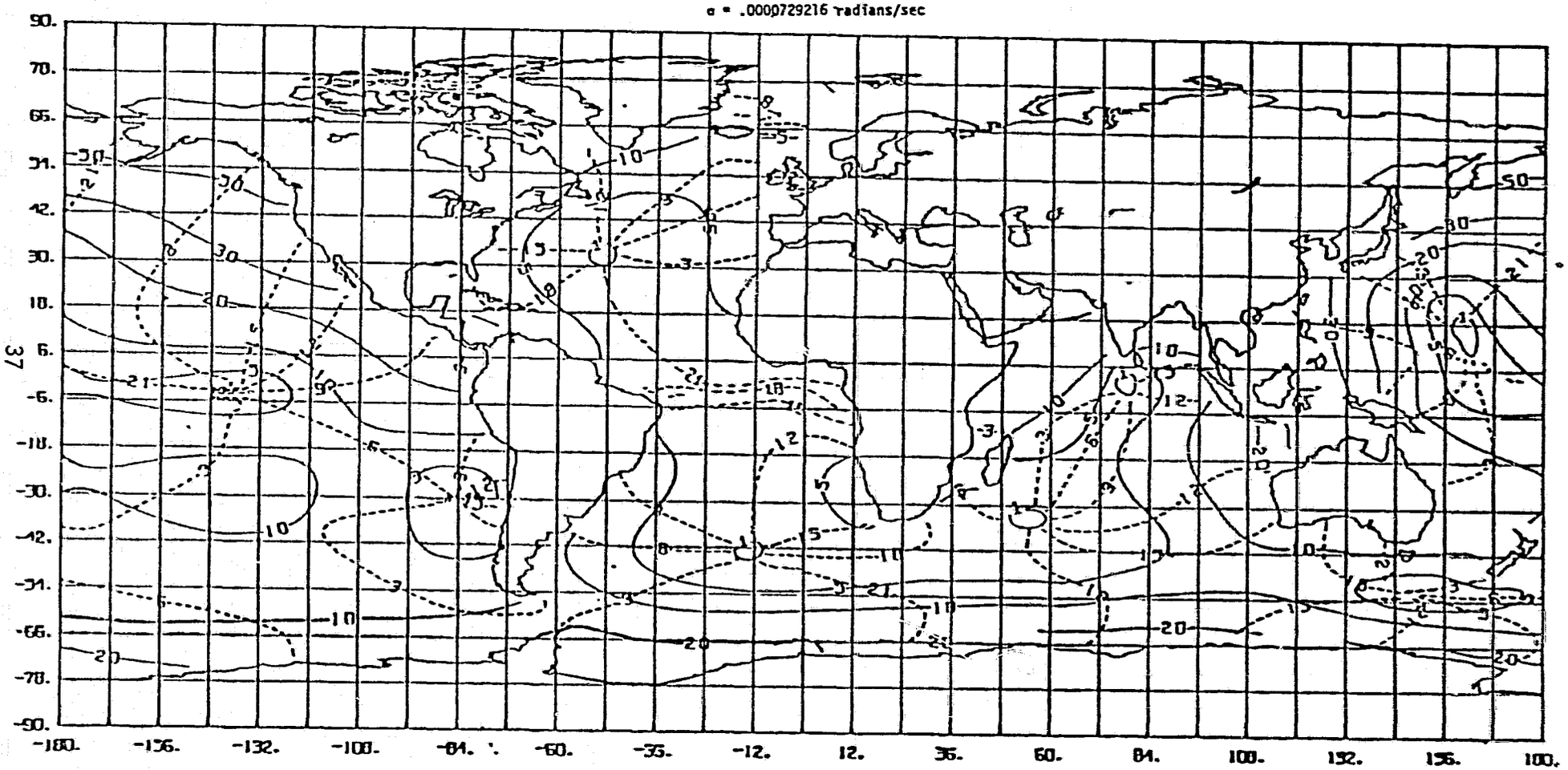

FIGURE 6: O_1 Tide Model neglecting ocean loading and self-gravitation effects integrated on a 3°x3° global grid.

ϕ: Dashed lines --- cotidal lines (phase) in hours

A: Solid lines —— corange lines (amplitude) in centimeters

$\xi(\phi,\lambda;t) = A(\phi,\lambda)\ cos[\sigma t-\phi]$

σ = .0000675983 radians/sec

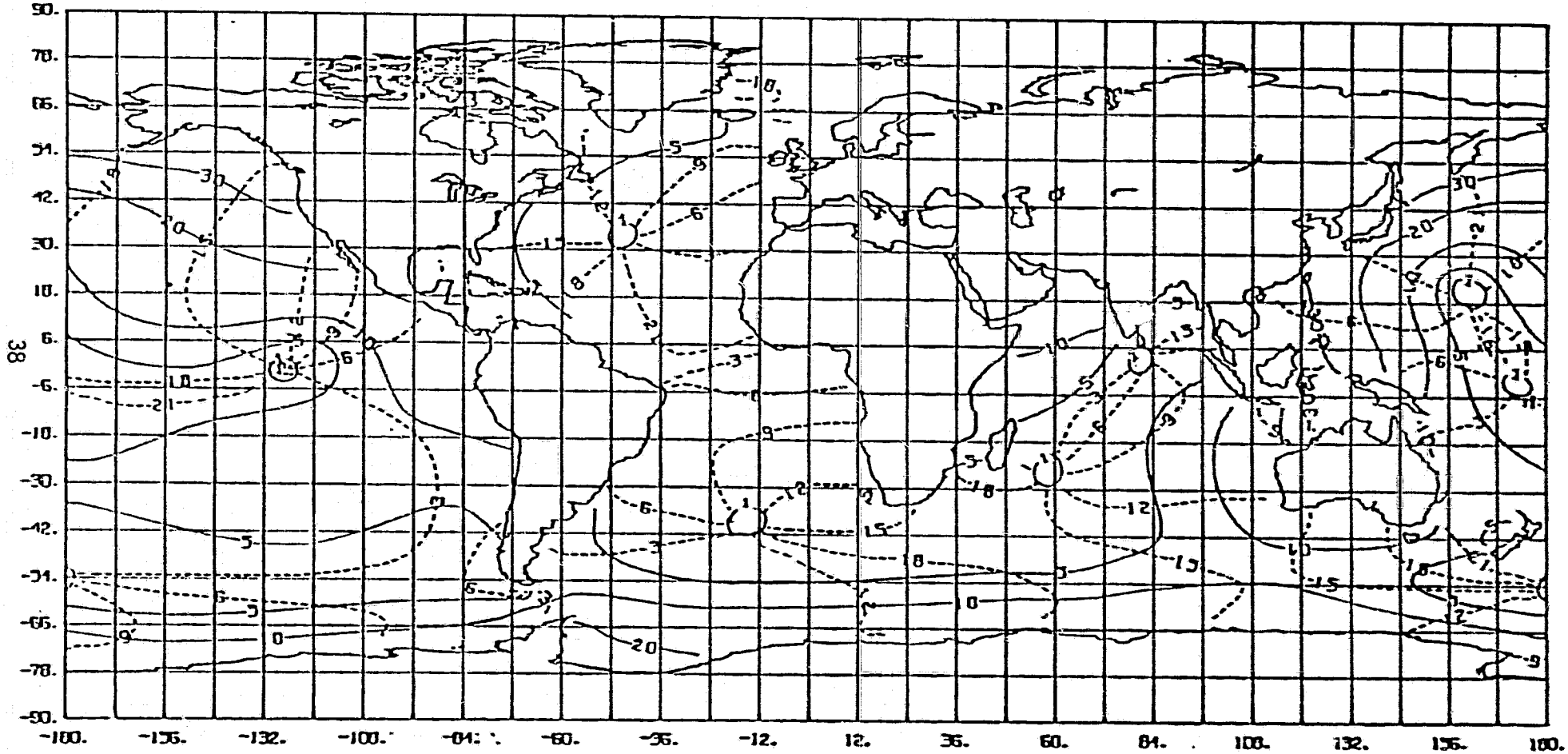

FIGURE 7: P_1 Tide Model neglecting ocean loading and self-gravitation effects integrated on a 3°x3° global grid.

ϕ: Dashed lines --- cotidal lines (phase) in hours

A: Solid lines —— corange lines (amplitude) in centimeters

$\xi(\phi,\lambda;t) = A(\phi,\lambda)\ cos[\sigma t-\phi]$

σ = .0000725236 radians/sec

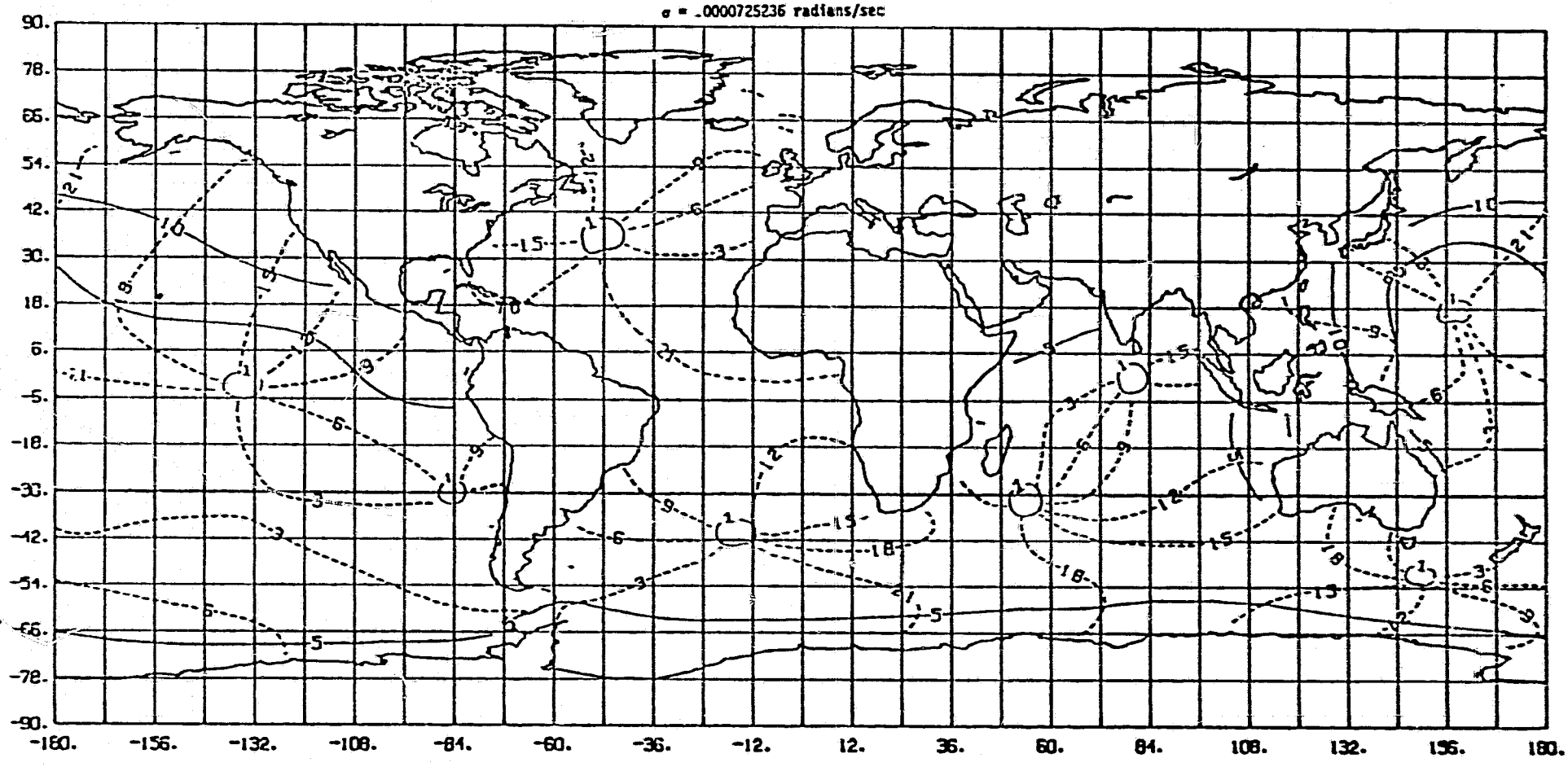

Figure 8

$3^{\circ} \times 3^{\circ}$ M_2 Vertical Displacement

Δ: Dashed Lines ---- cotidal lines (phase) in hours

A: Solid Lines —— corange lines (amplitude) in millimeters

$U(\phi,\lambda;\tau) = A(\phi,\lambda) \cos [\sigma(\tau-\tau_0) - \Delta + \varepsilon]$

$\sigma = .00014052$

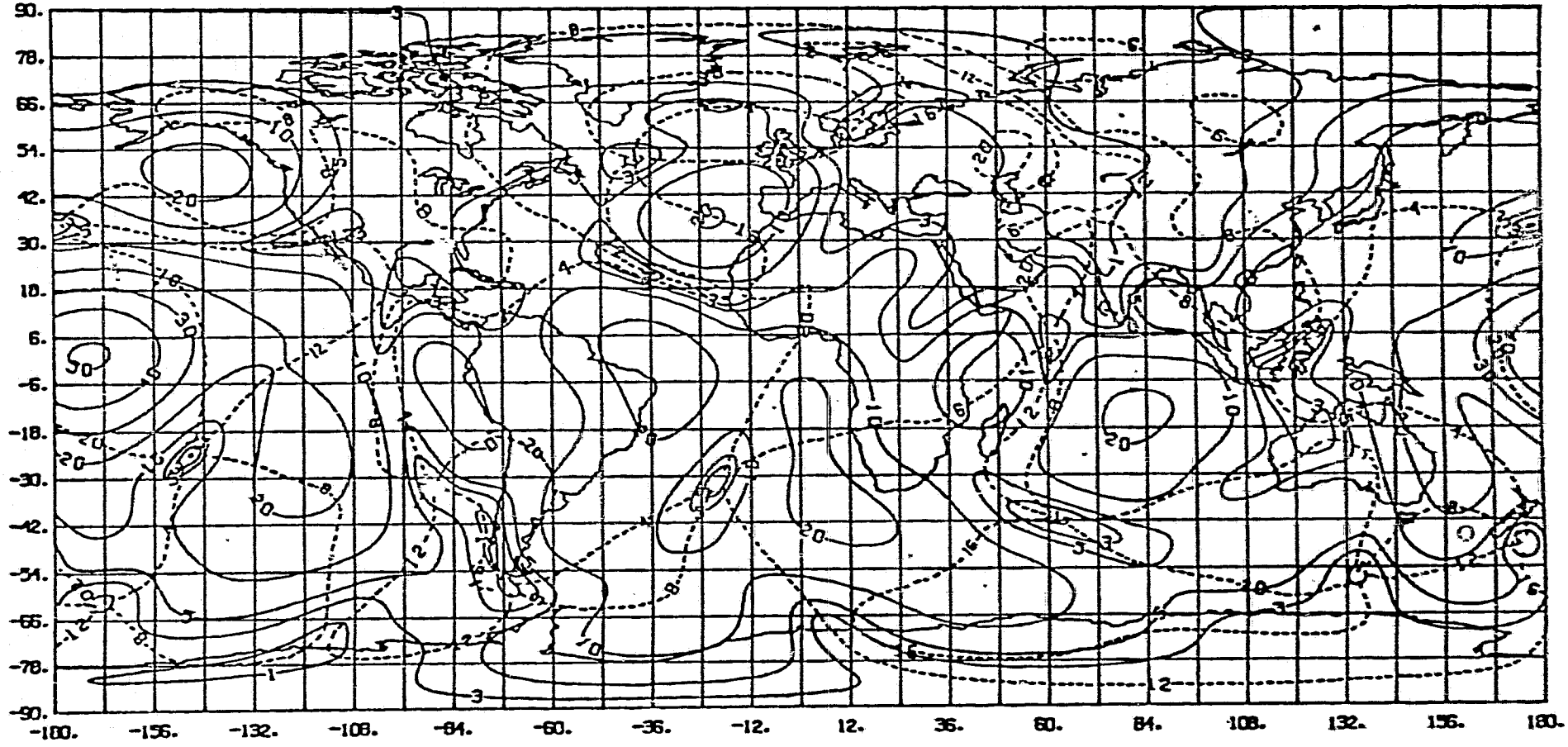

Figure 9

$3^{\circ} \times 3^{\circ}$ S_2 Vertical Displacement

Δ: Dashed Lines ---- cotidal lines (phase) in hours

A: Solid Lines —— corange lines (amplitude) in millimeters

$U(\phi,\lambda;\tau) = A(\phi,\lambda) \cos [\sigma(\tau-\tau_o) - \Delta + \varepsilon]$

$\sigma = .00014544$

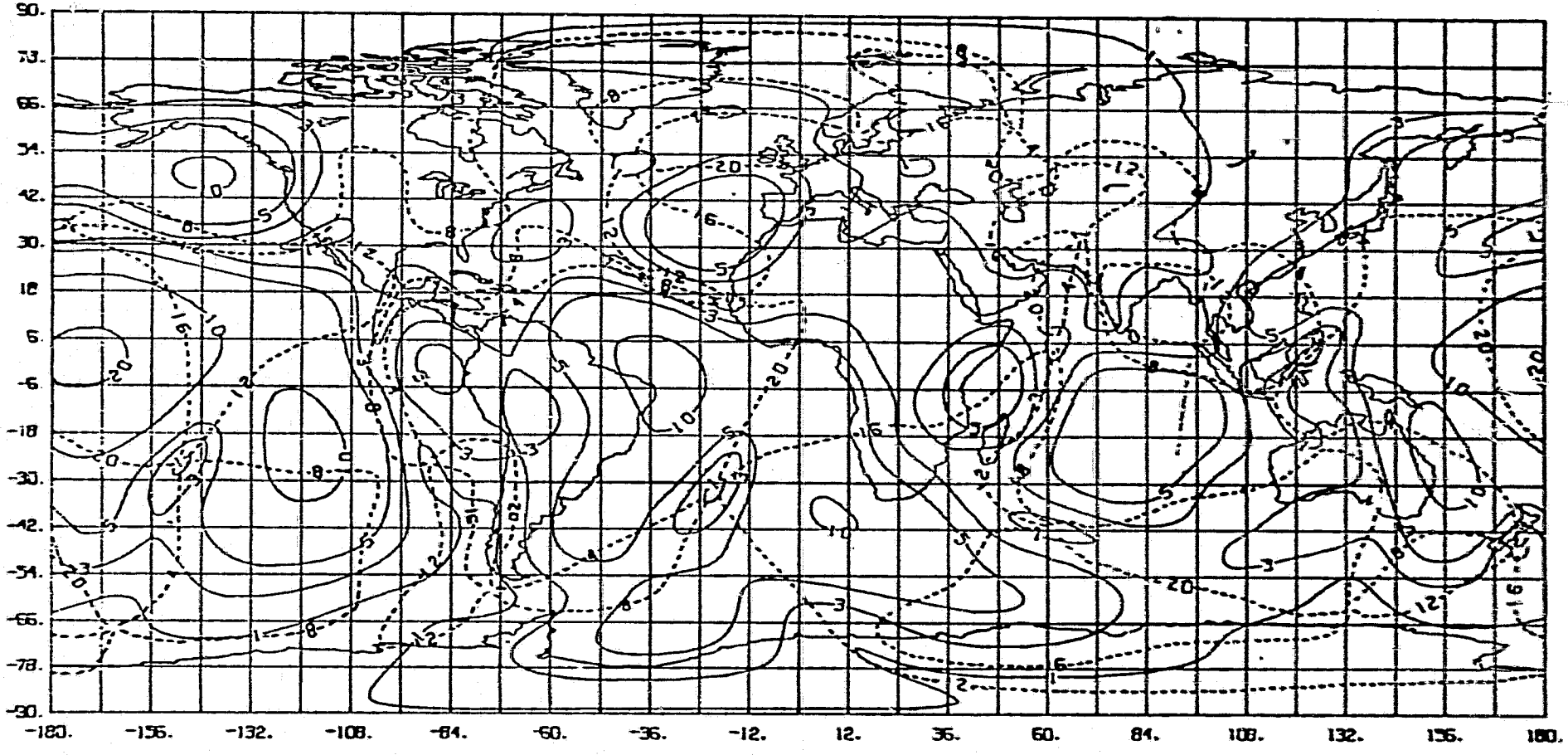

Figure 10

$3^{\circ} \times 3^{\circ}$ N_2 Vertical Displacement

Δ: Dashed Lines ---- cotidal lines (phase) in hours

A: Solid Lines —— corange lines (amplitude) in millimeters

$$U(\phi,\lambda;\tau) = A(\phi,\lambda) \cos [\sigma(\tau-\tau_0) - \Delta + \varepsilon]$$

$$\sigma = .00013788$$

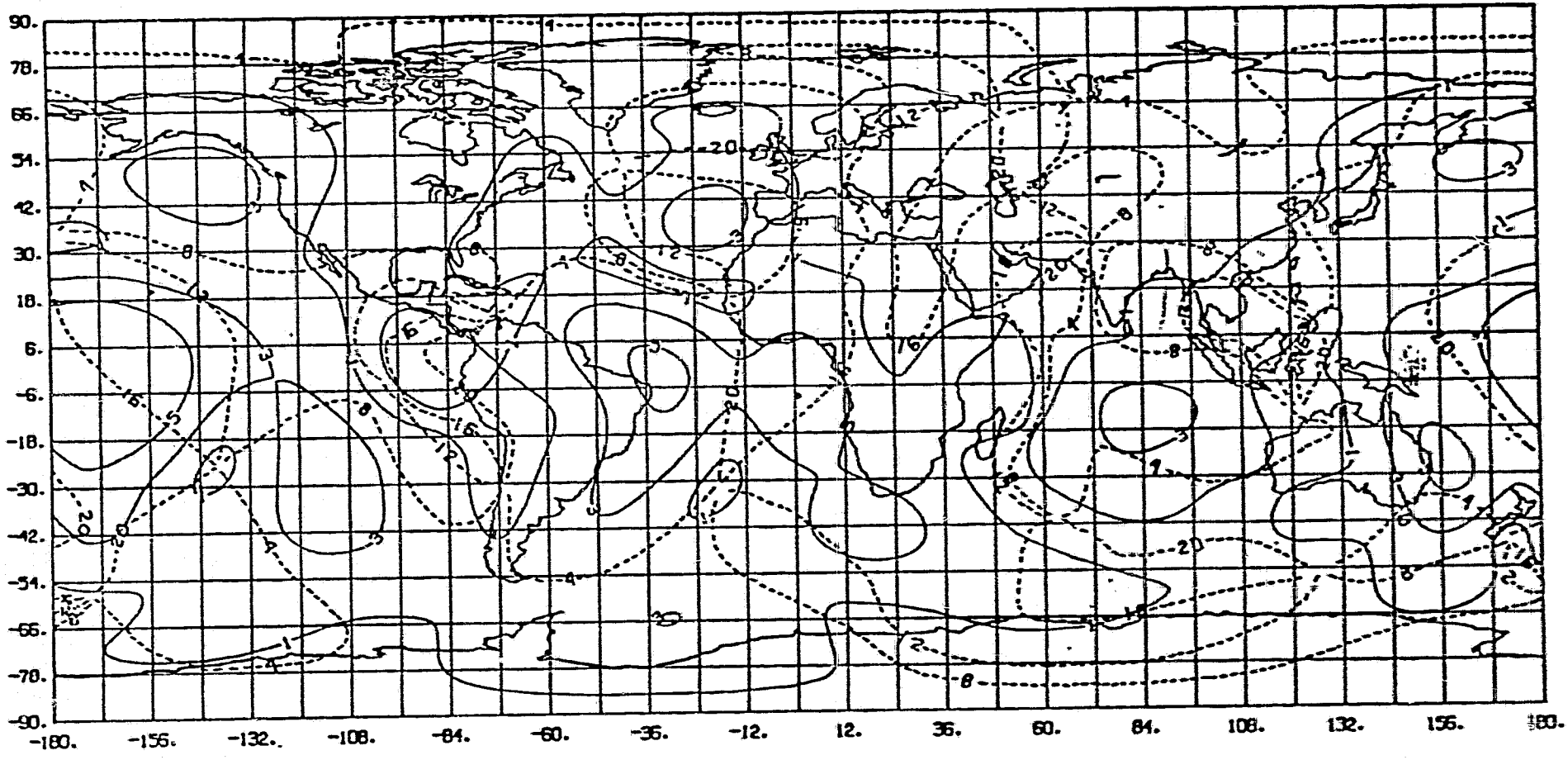

Figure 11

$3^{\circ} \times 3^{\circ}$ K_2 Vertical Displacement

A: Dashed Lines ---- cotidal lines (phase) in hours

A: Solid Lines —— corange lines (amplitude) in millimeters

$$U(\phi,\lambda;\tau) = A(\phi,\lambda) \cos [\sigma(\tau-\tau_0) - \Delta + \varepsilon]$$

$$\sigma = .00014584$$

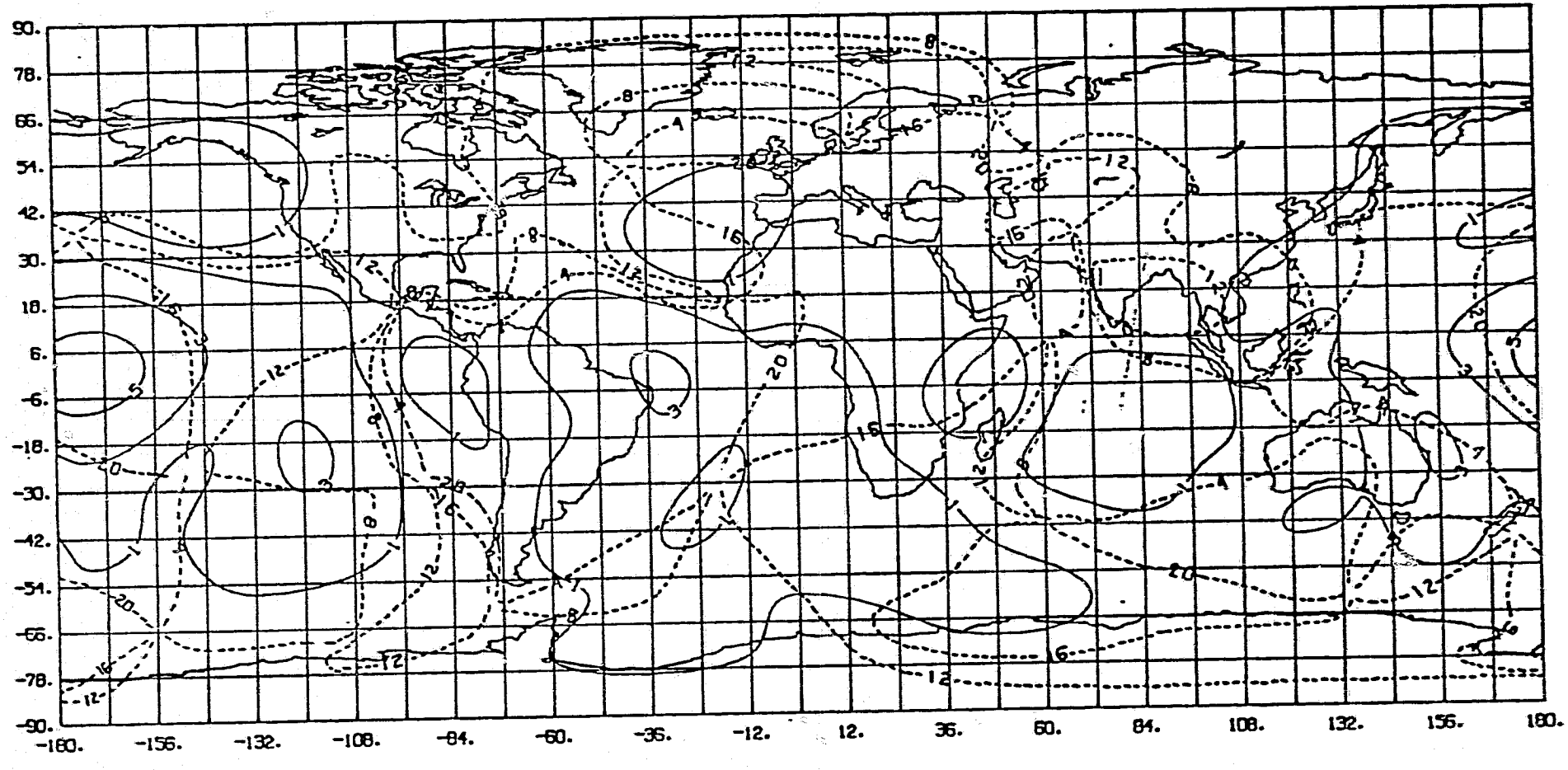

Figure 12

$3^\circ \times 3^\circ$ K_1 Vertical Displacement

Δ: Dashed Lines ----- cotidal lines (phase) in hours

A: Solid Lines —— corange lines (amplitude) in millimeters

$U(\phi,\lambda;\tau) = A(\phi,\lambda) \cos [\sigma(\tau-\tau_0) - \Delta + \varepsilon]$

$\sigma = .00007292$

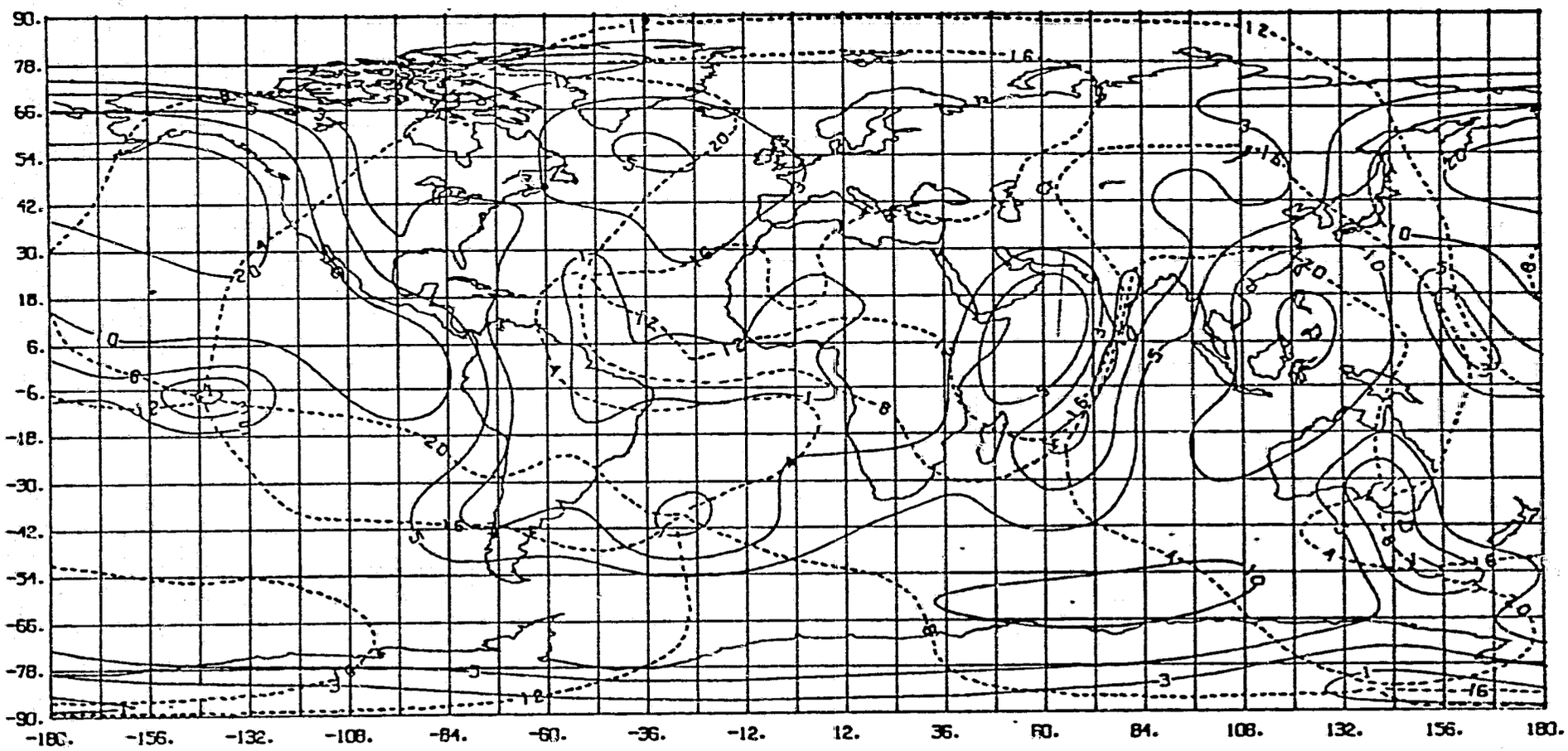

Figure 13

$3^\circ \times 3^\circ$ O_1 Vertical Displacement

Δ: Dashed Lines ---- cotidal lines (phase) in hours

A: Solid Lines —— corange lines (amplitude) in millimeters

$U(\phi,\lambda;\tau) = A(\phi,\lambda) \cos [\sigma(\tau-\tau_0) - \Delta + \varepsilon]$

$\sigma = .00006760$

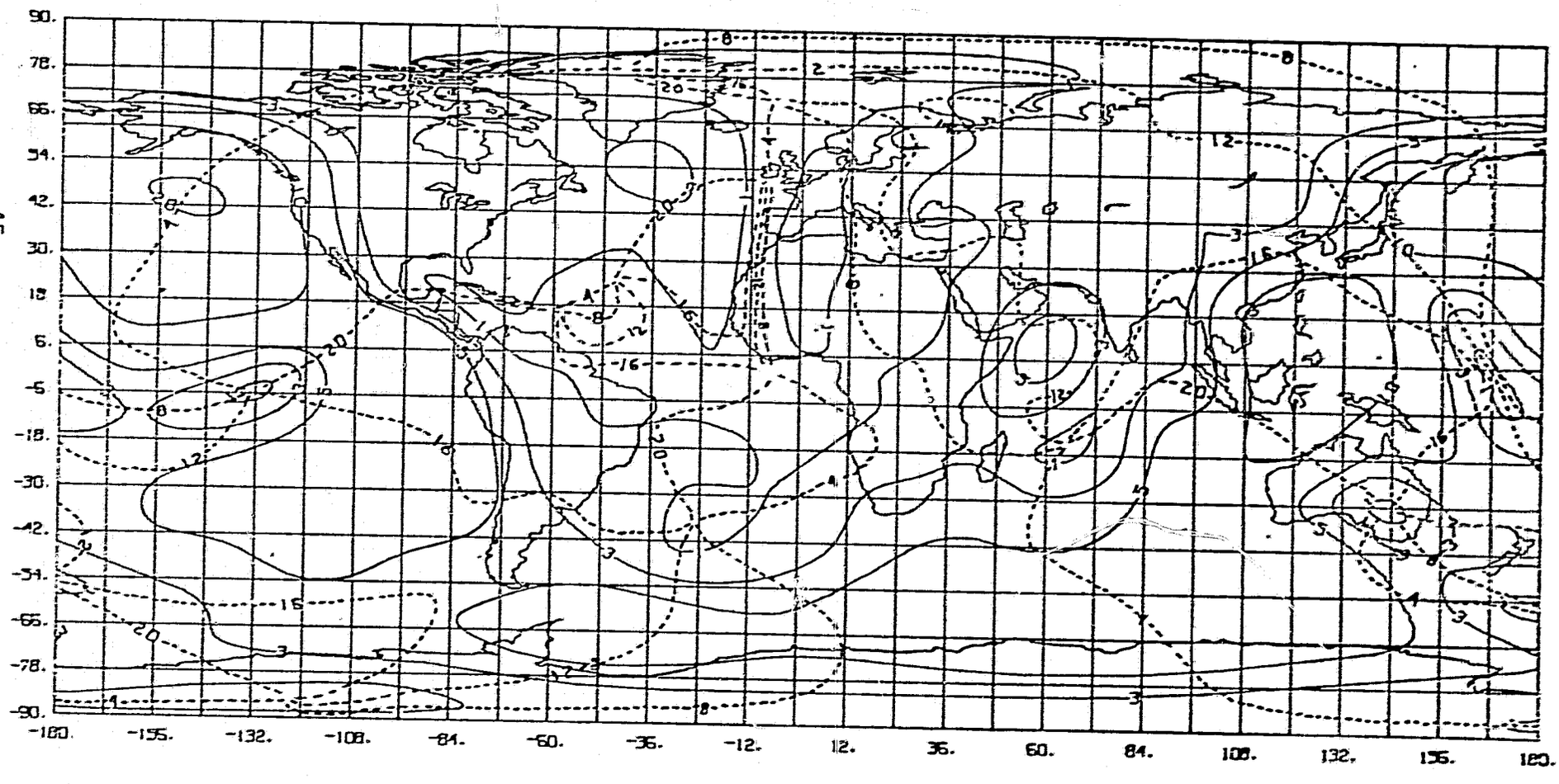

Figure 14

$3^{\circ} \times 3^{\circ}$ P_1 Vertical Displacement

Δ: Dashed Lines ---- cotidal lines (phase) in hours

A: Solid Lines —— corange lines (amplitude) in millimeters

$$U(\phi,\lambda;\tau) = A(\phi,\lambda) \cos [\sigma(\tau-\tau_0) - \Delta + \varepsilon]$$

$$\sigma = .00007252$$

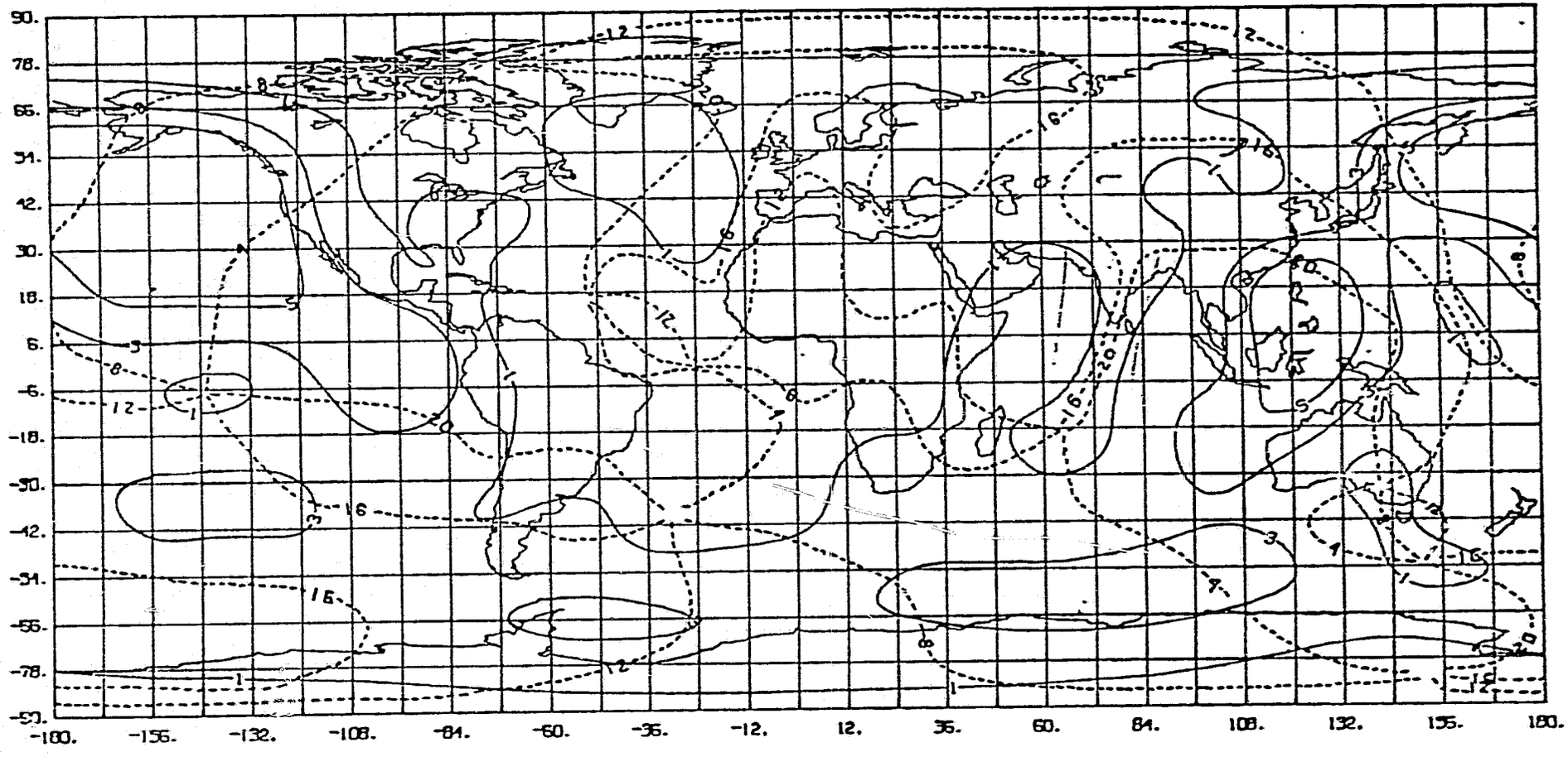

Figure 15

3^{o} x 3^{o} M_2 Horizontal Displacement in $\hat{\theta}$ Direction

Δ: Dashed Lines ---- cotidal lines (phase) in hours

A: Solid Lines —— corange lines (amplitude) in tenths of millimeters

$V_{\theta}(\phi,\lambda;\tau) = A(\sigma,\lambda) \cos [\sigma(\tau-\tau o) - \Delta + \varepsilon]$

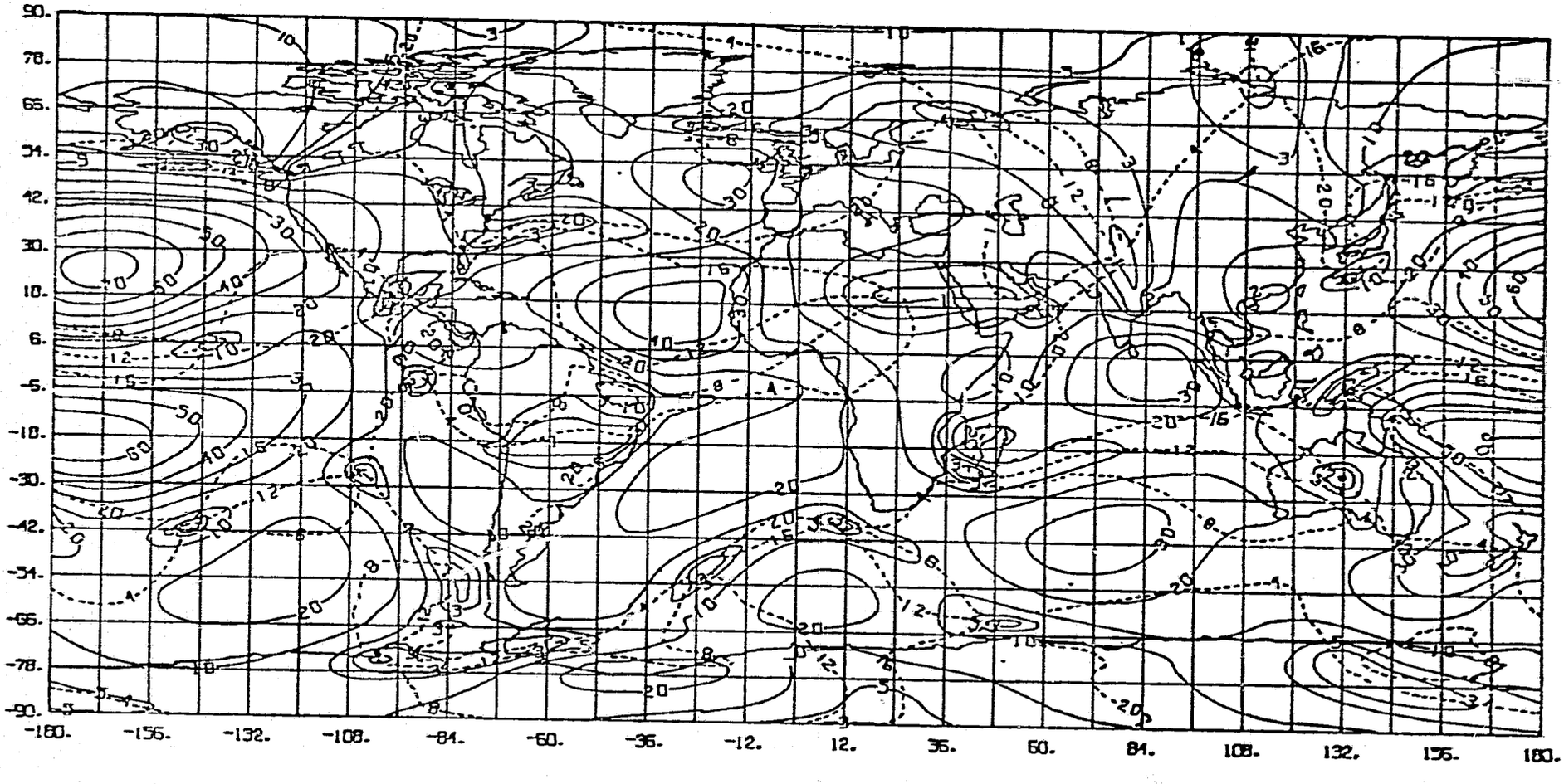

Figure 16

$3^{\circ} \times 3^{\circ}$ M_2 Horizontal Displacement in $\hat{\lambda}$ Direction

Δ: Dashed Lines ---- cotidal lines (phase) in hours

A: Solid Lines —— corange lines (amplitude) in tenths of millimeters

$$V_{\lambda}(\phi,\lambda;\tau) = A(\phi,\lambda) \cos [\sigma(\tau-\tau o) - \Delta + \varepsilon]$$

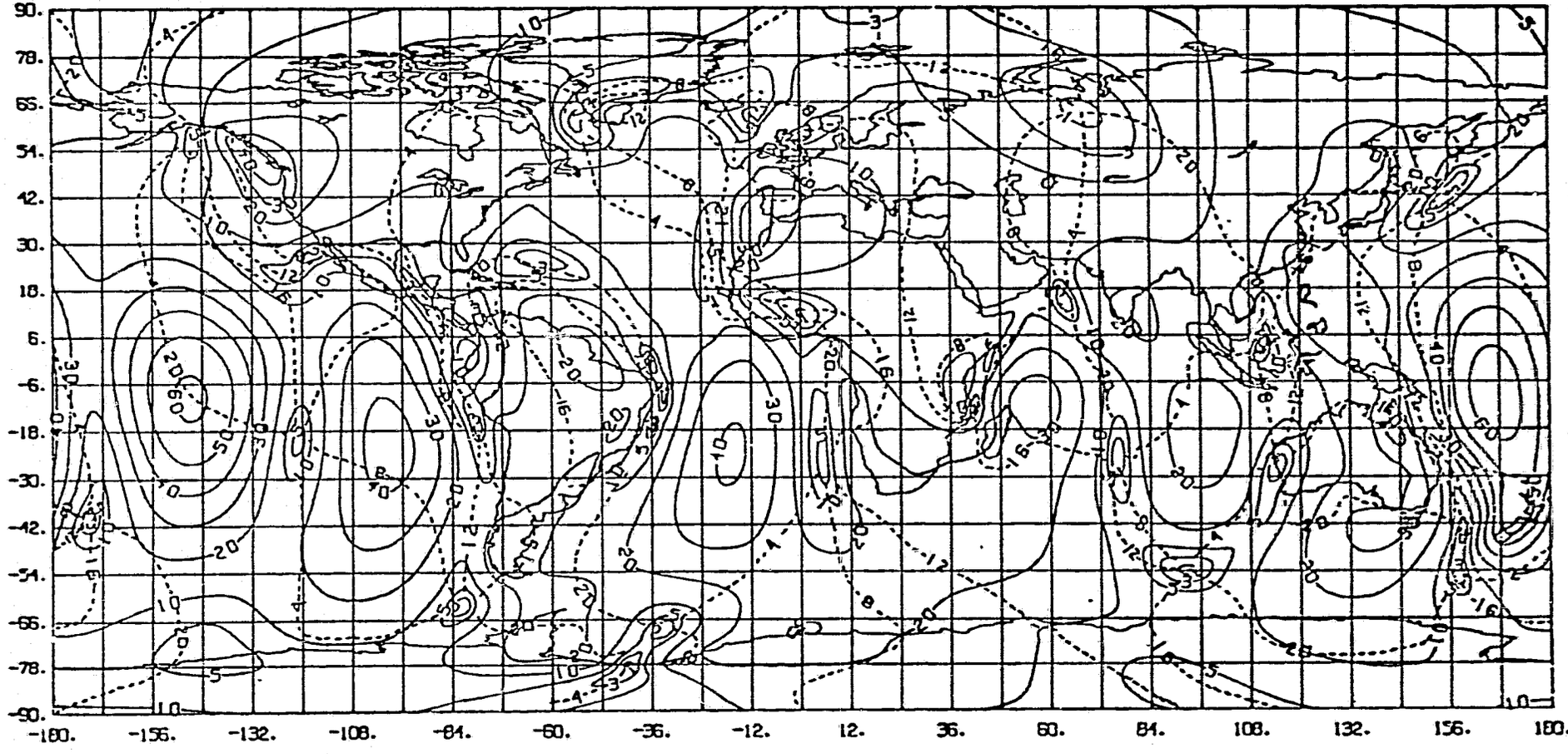

Figure 17

$3^\circ \times 3^\circ$ M_2 Newtonian Gravity Acceleration

Δ: Dashed Lines ---- phase lines in hours

A: Solid Lines —— amplitude lines in tenths of microgals

$$g(\phi,\lambda;\tau) = A(\phi,\lambda) \cos [\sigma(\tau-\tau_0) - \Delta + \varepsilon]$$

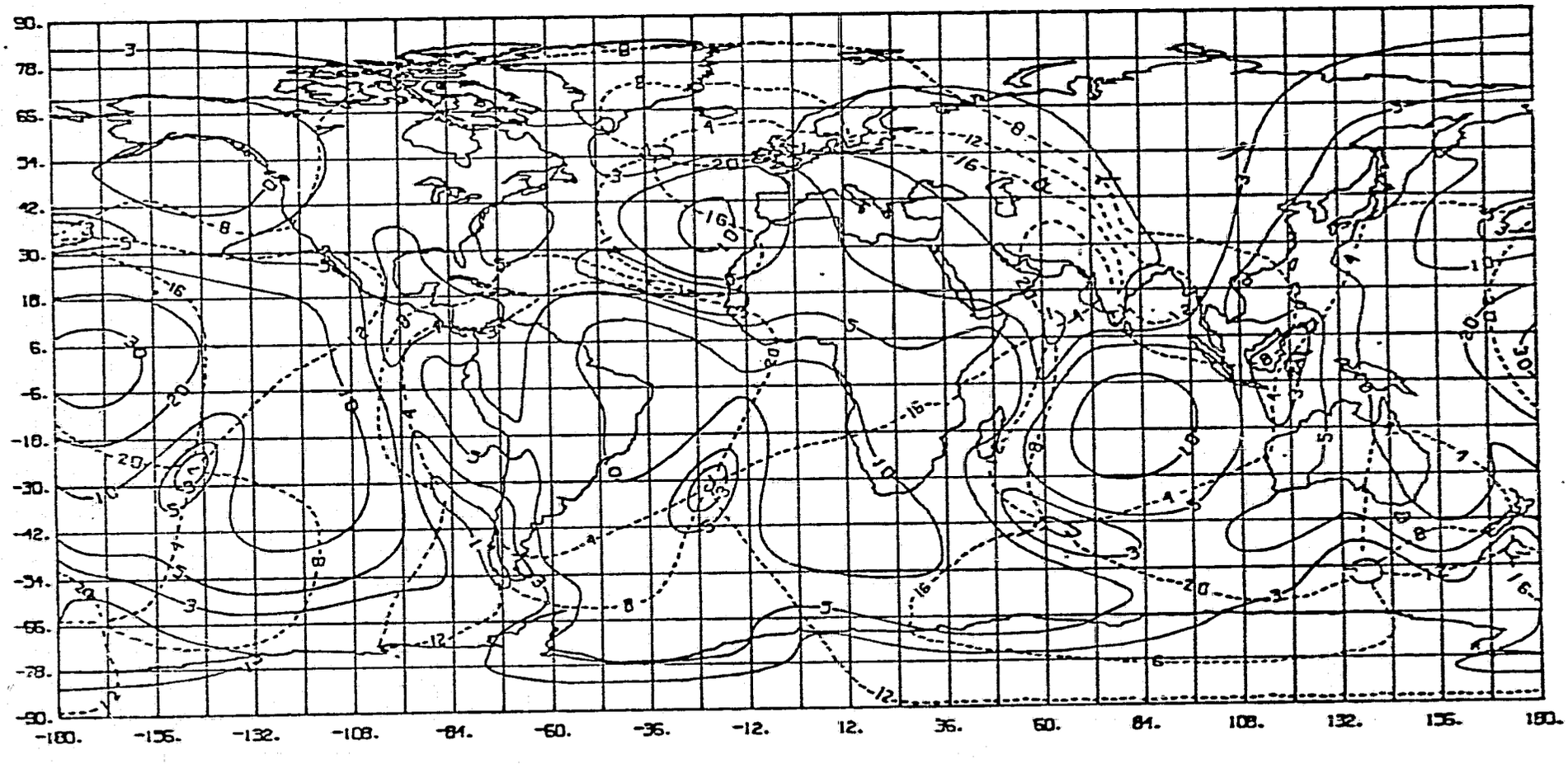

Figure 18

3^{o} x 3^{o} M_2 Elastic Gravity Acceleration

Δ: Dashed Lines ----- phase lines in hours

A: Solid Lines —— amplitude lines in tenths of microgals

$g(\phi,\lambda;\tau) = A(\phi,\lambda) \cos [\sigma(\tau-\tau_0) - \Delta + \varepsilon]$

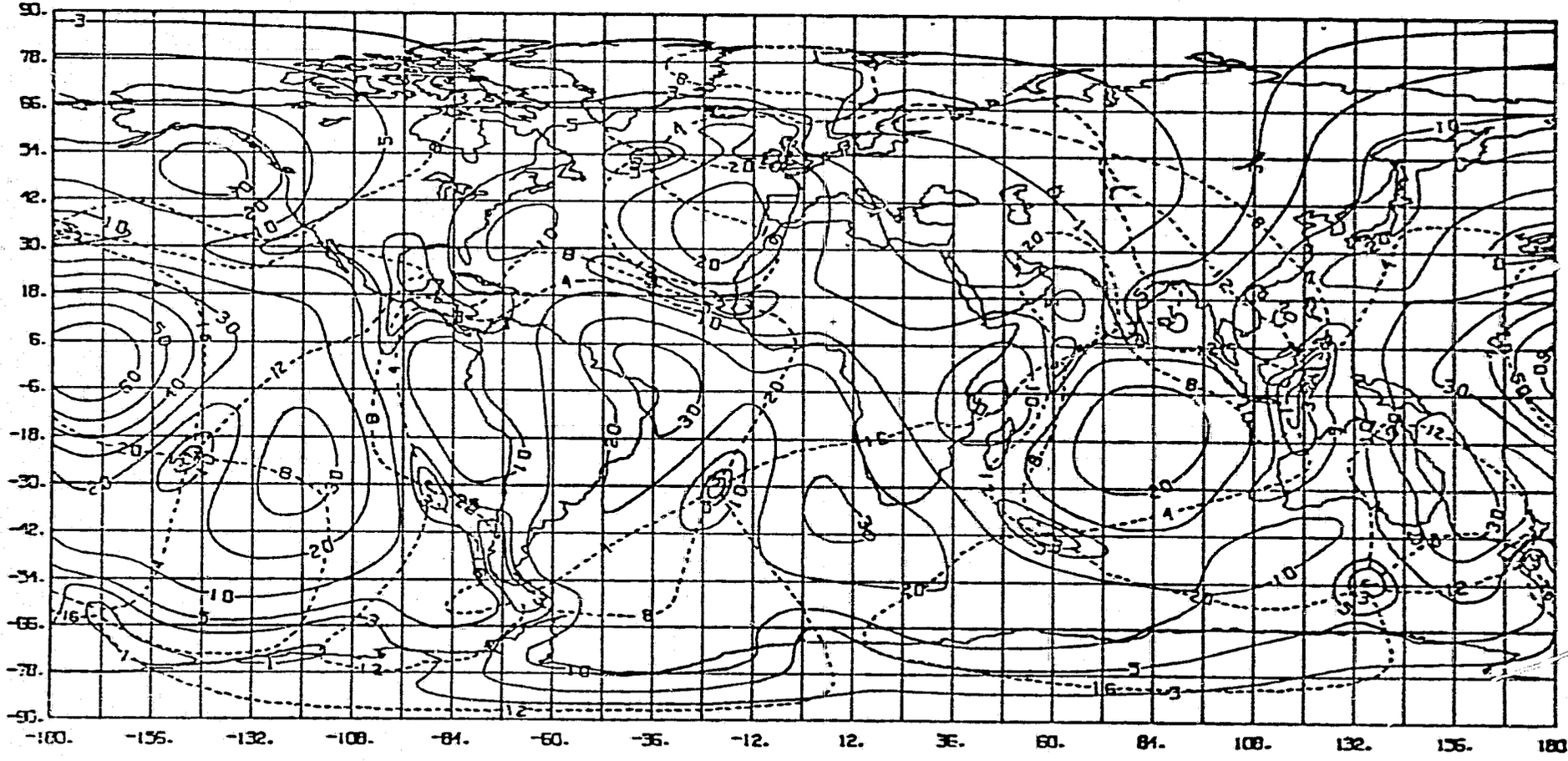

Figure 19

$3^\circ \times 3^\circ$ O_1 Newtonian Gravity Acceleration

Δ: Dashed Lines - - - - phase lines in hours

A: Solid Lines —— amplitude lines in tenths of microgals

$$g(\phi,\lambda;\tau) = A(\phi,\lambda) \cos [\sigma(\tau-\tau_o) - \Delta + \varepsilon]$$

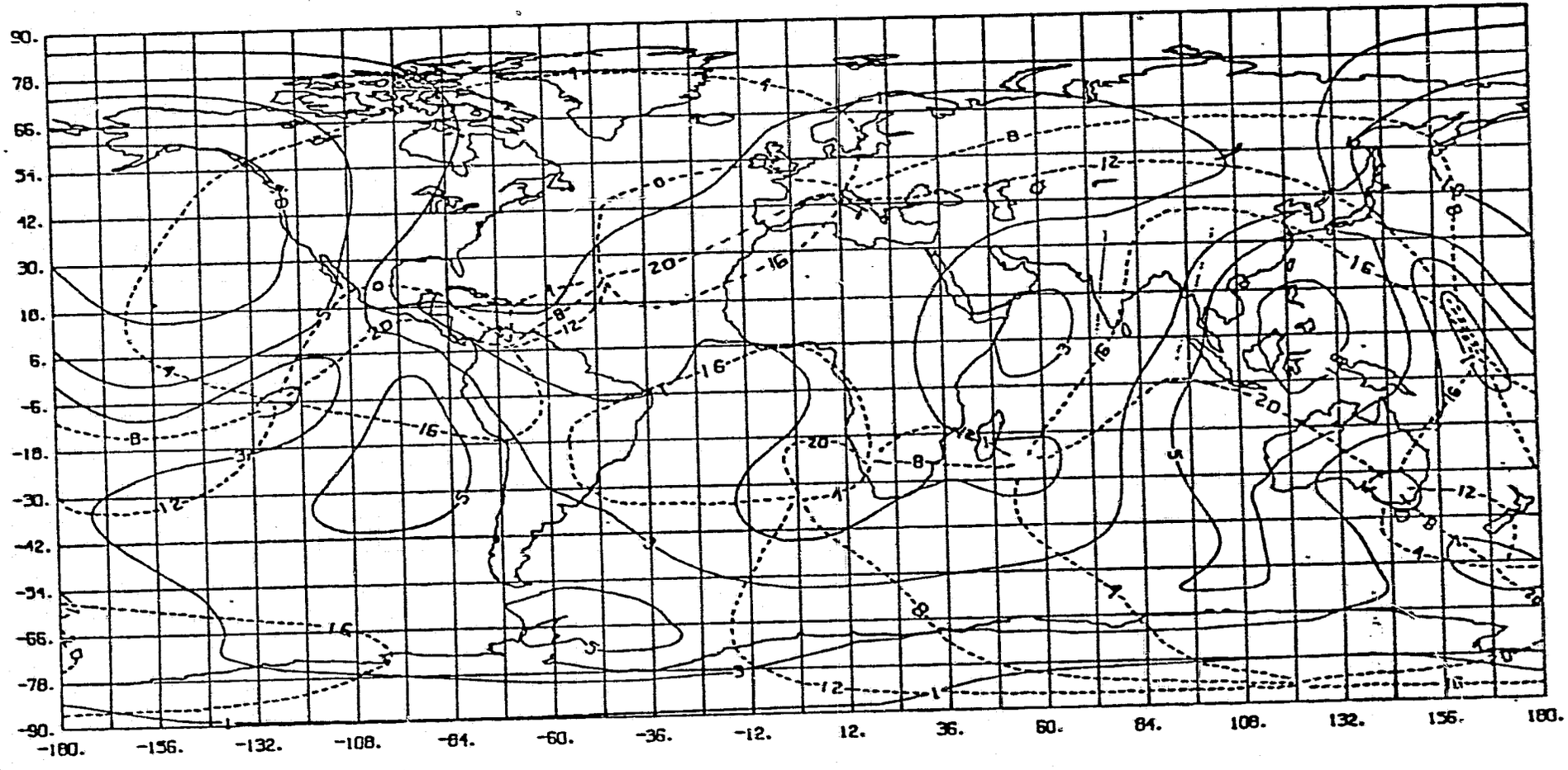

Figure 20

$3^{o} \times 3^{o}$ O_1 Elastic Gravity Acceleration

Δ: Dashed Lines ---- phase lines in hours

A: Solid Lines —— amplitude lines in tenths of microgals

$$g(\phi,\lambda;\tau) = A(\phi,\lambda) \cos [\sigma(\tau-\tau_o) - \Delta + \varepsilon]$$

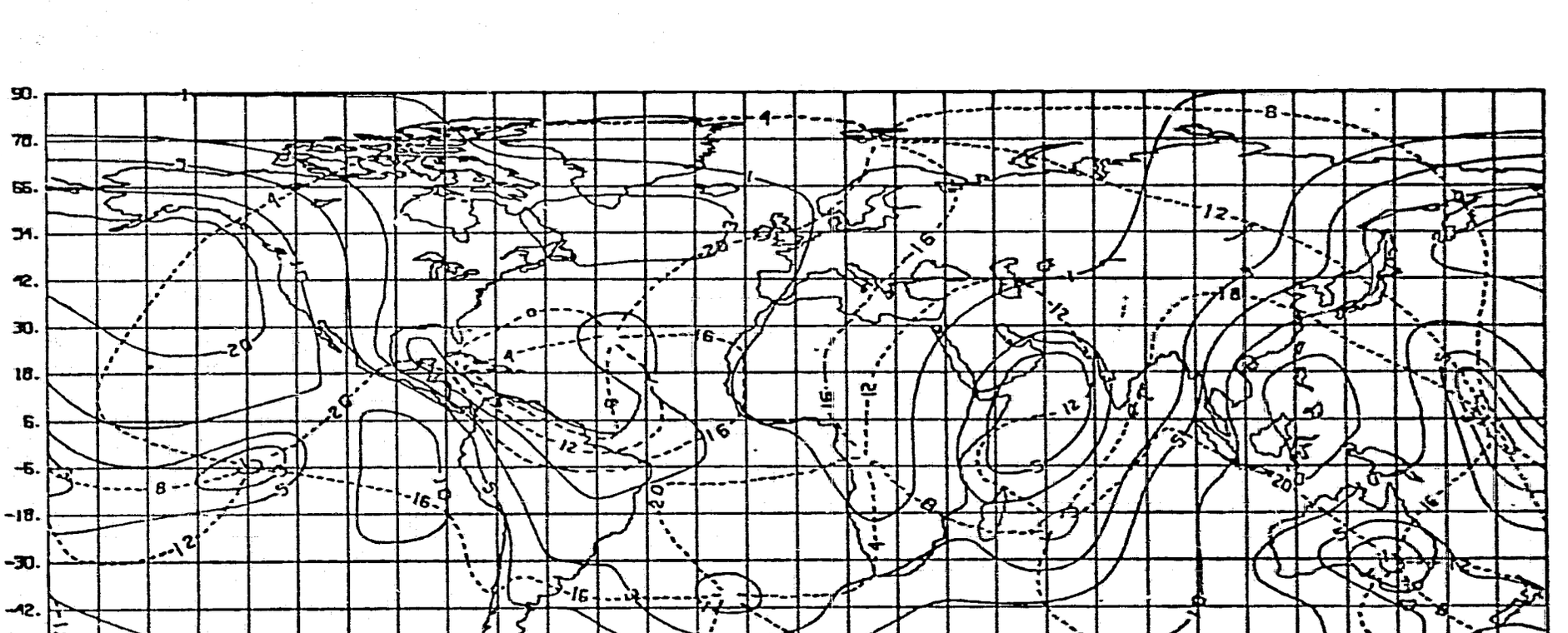

Figure 21

3° x 3° e_{rr} , Radial Strain Component

Δ: Dashed Lines --- cotidal lines (phase) in hours

A: Solid Lines —— corange lines (amplitude) ($\times 10^{-11}$)

$e_{rr}(\phi,\lambda;\tau) = A(\phi,\lambda)\cos[\sigma(\tau-\tau_0)-\Delta+\varepsilon]$

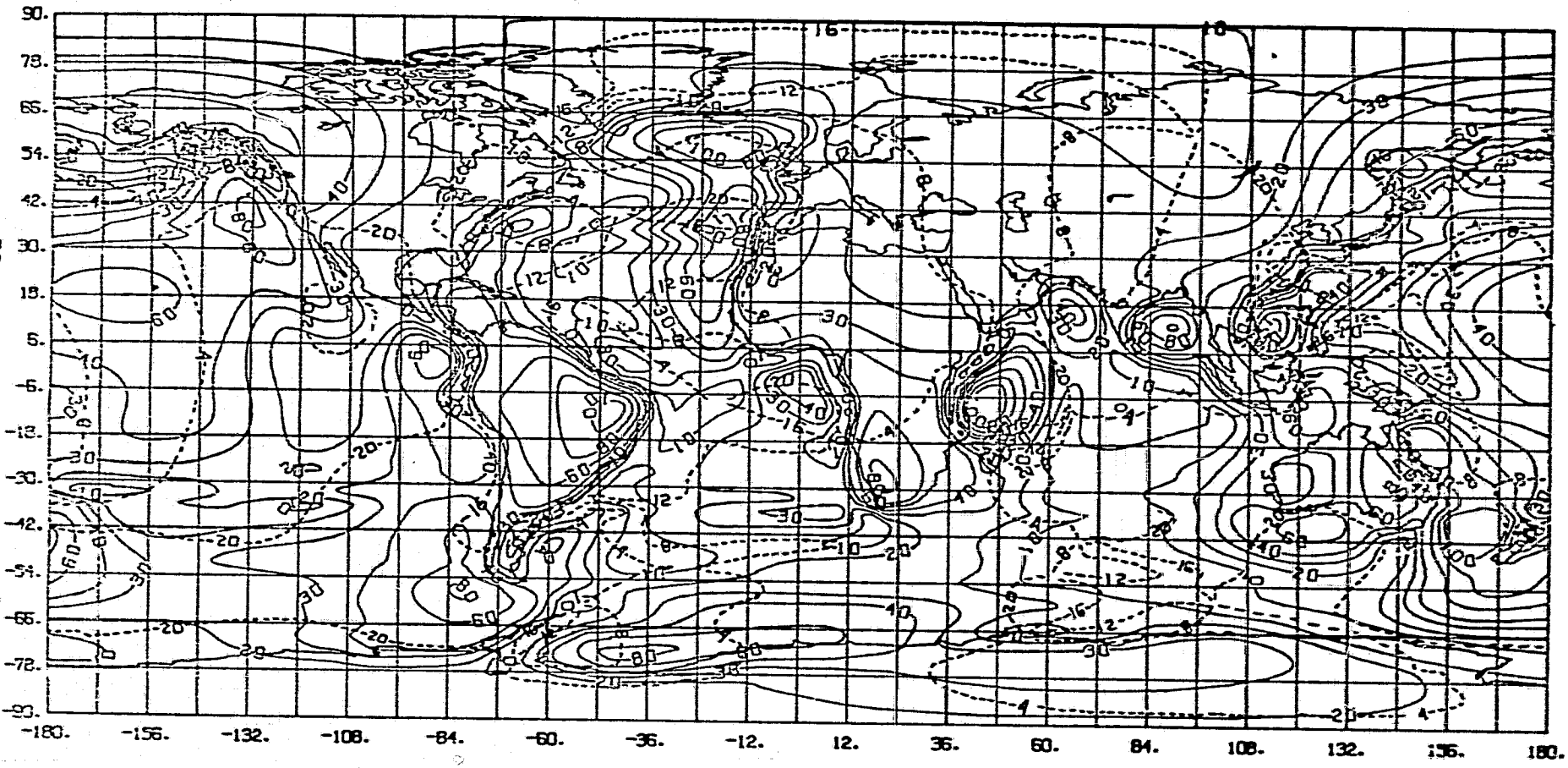

Figure 22

3° x 3° $e_{\theta\theta}$, Horizontal Surface Strain Component over the Ocean

Δ: Dashed Lines --- cotidal lines (phase) in hours

A: Solid Lines —— corange lines (amplitude) ($x10^{-9}$)

$e_{\theta\theta}(\phi,\lambda;\tau) = A(\phi,\lambda)\ \cos[\sigma(\tau-\tau_0)-\Delta+\epsilon]$

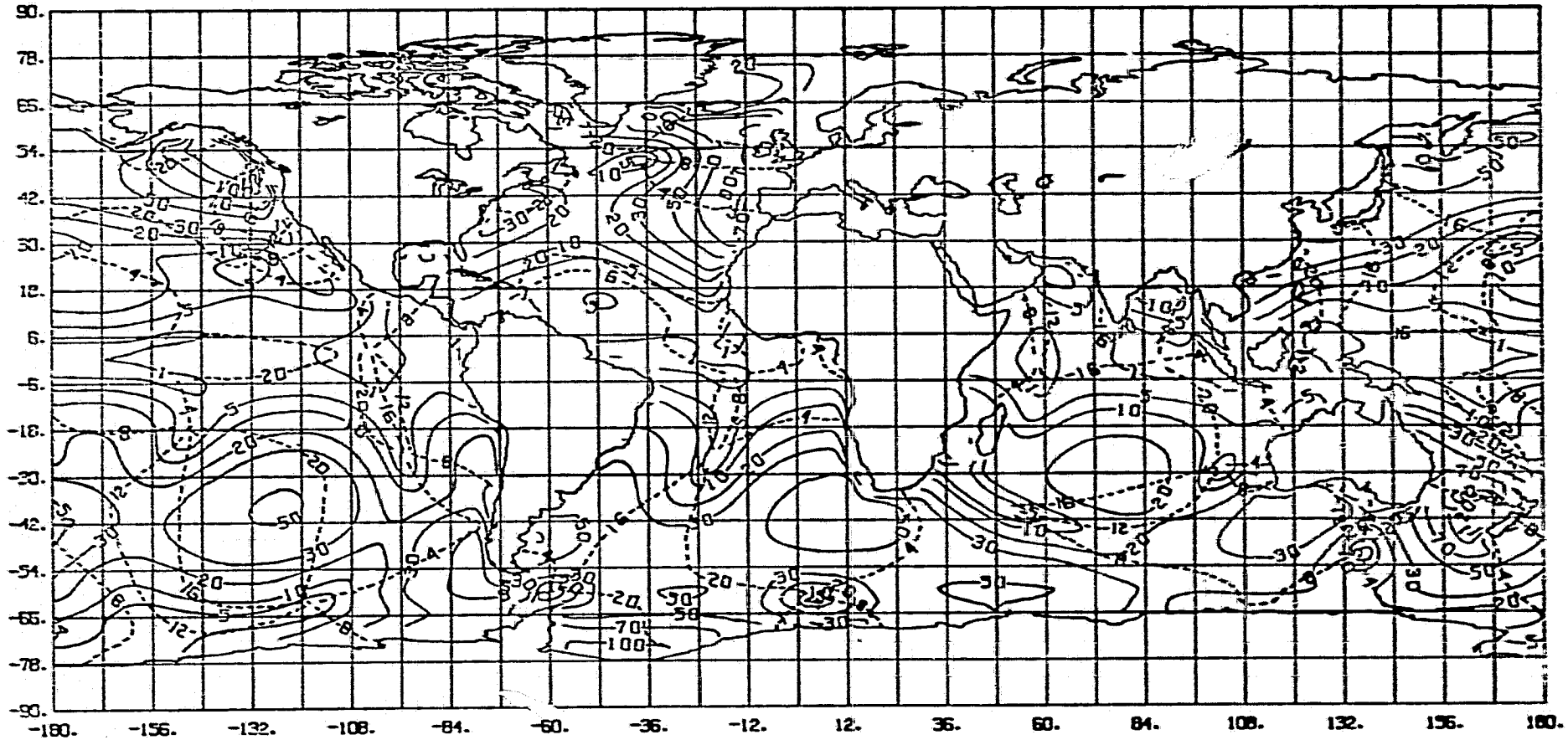

Figure 23

3° x 3° $e_{\theta\theta}$, Horizontal Surface Strain Component over Land

Δ: Dashed lines --- cotidal lines (phase) in hours

A: Solid lines —— corange lines (amplitude) ($x10^{-10}$)

$e_{\theta\theta}(\phi,\lambda;\tau) = A(\phi,\lambda)\cos[\sigma(\tau-\tau_0)-\Delta+\epsilon]$

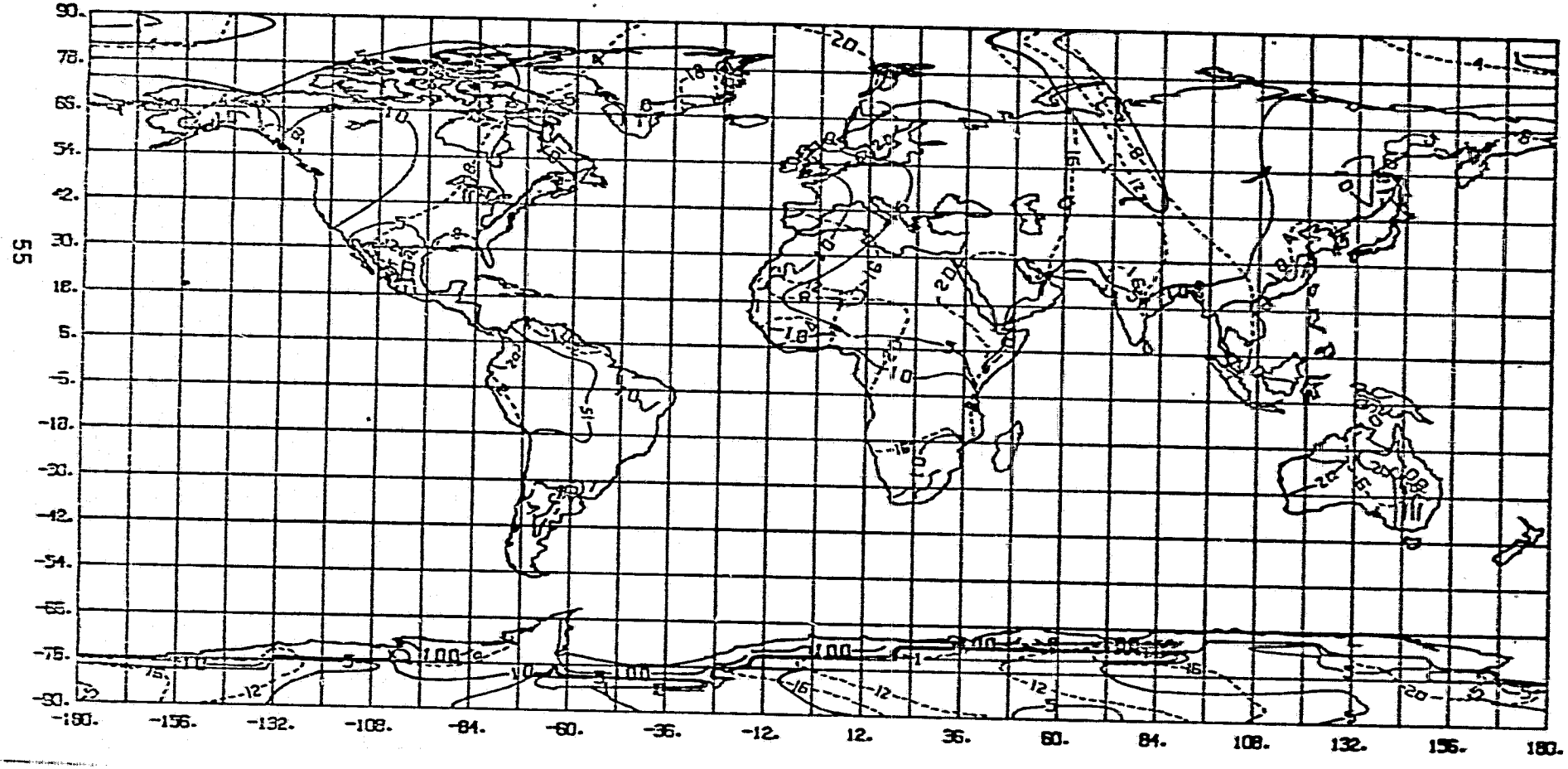

Figure 24

$3° \times 3°$ $e_{\lambda\lambda}$, Horizontal Surface Strain Component over the Ocean

Δ: Dashed lines --- cotidal lines (phase) in hours

A: Solid lines —— corange lines (amplitude)($\times 10^{-9}$)

$$e_{\lambda\lambda}(\phi,\lambda;\tau) = A(\phi,\lambda)\cos[\sigma(\tau-\tau_0)-\Delta+\varepsilon]$$

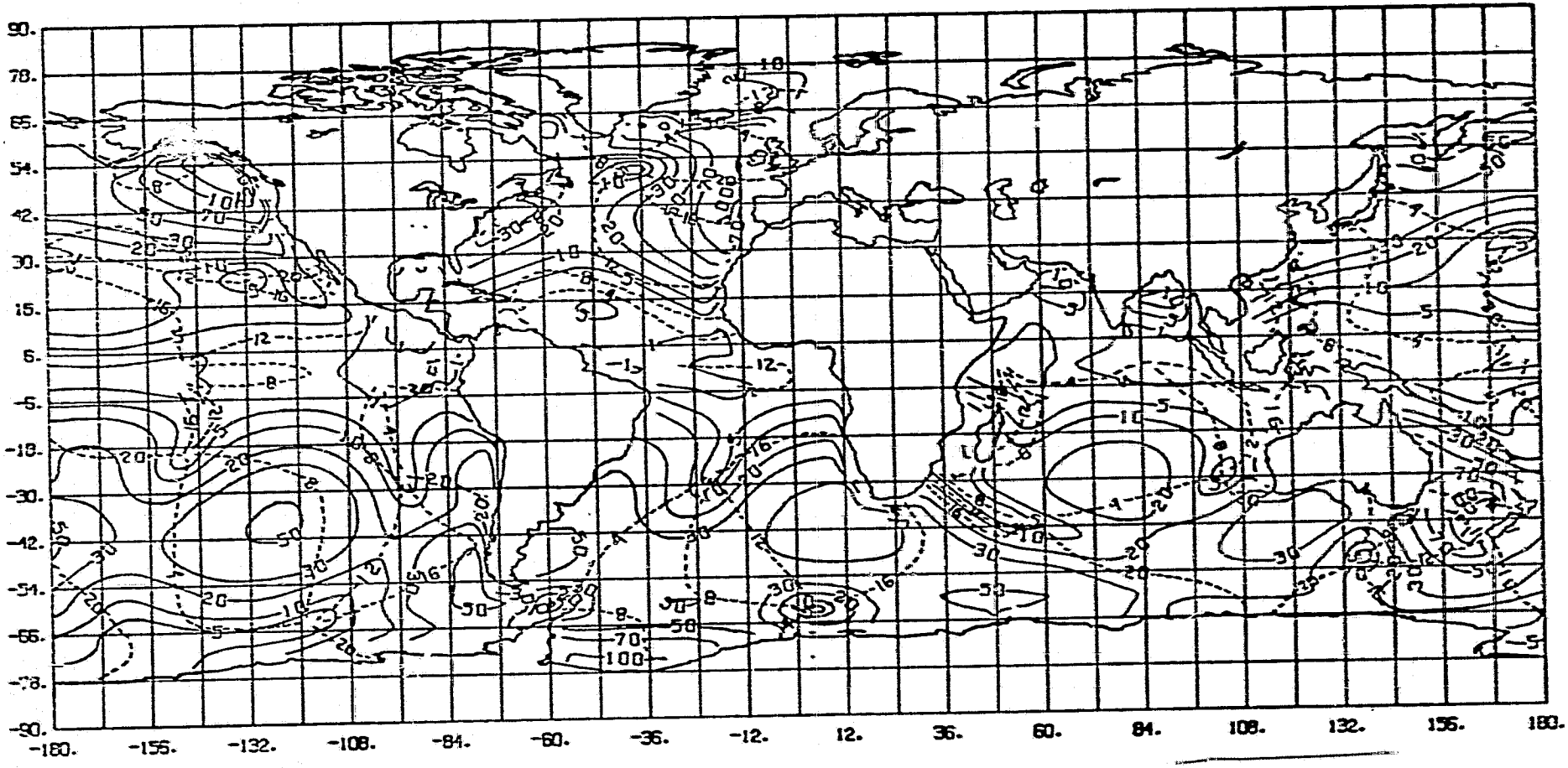

Figure 25

3° x 3° $e_{\lambda\lambda}$, Horizontal Surface Strain Component over Land

Δ: Dashed Lines --- cotidal lines (phase) in hours

A: Solid Lines —— corange lines (amplitude) ($x10^{-10}$)

$e_{\lambda\lambda}(\phi,\lambda;\tau) = A(\phi,\lambda)\cos[\sigma(\tau-\tau_0)-\Delta+\epsilon]$

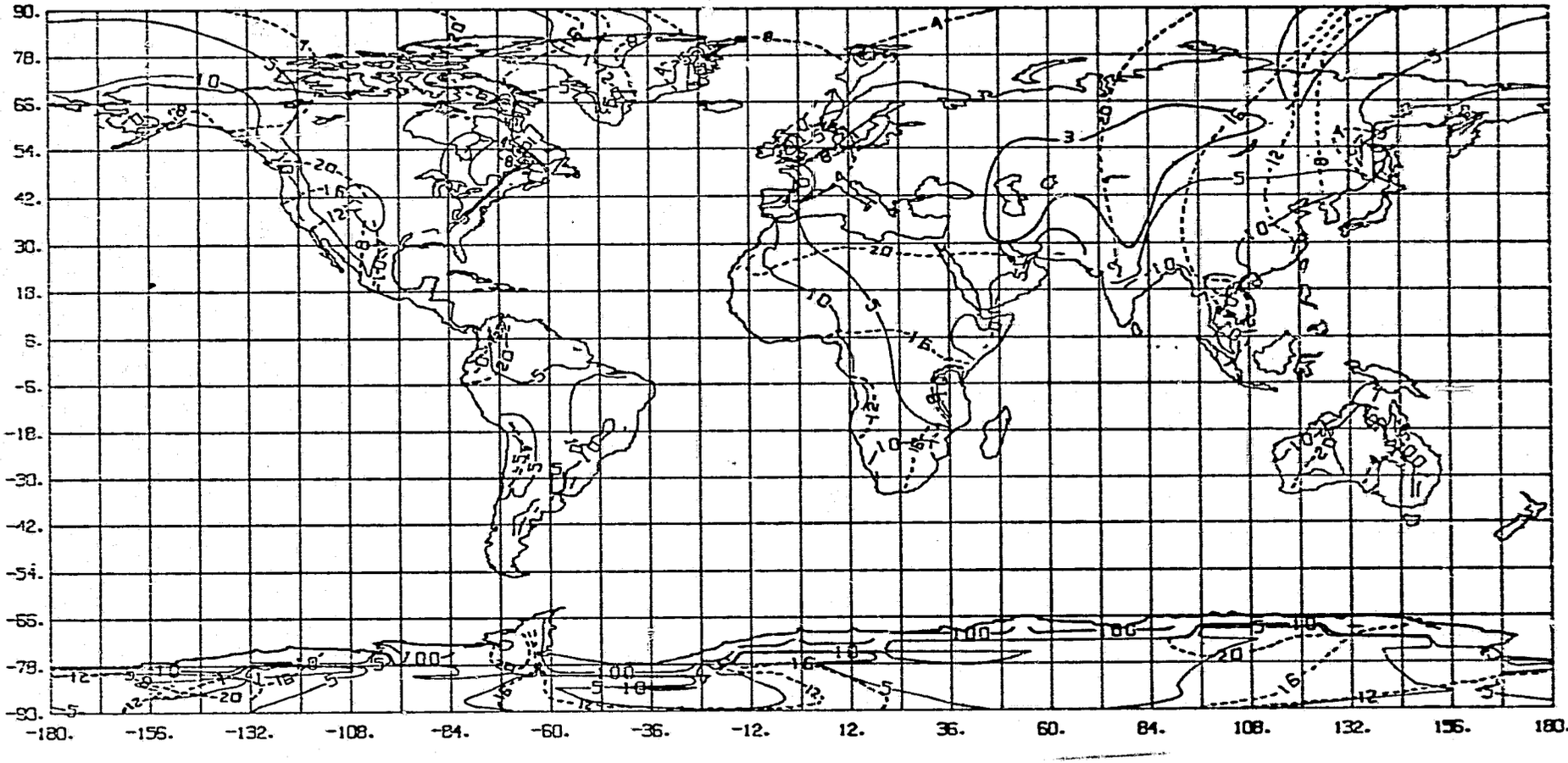

Figure 26

3° x 3° $e_{\lambda\theta}$, Horizontal Surface Strain Component over the Ocean

∇: Dashed lines --- cotidal lines (phase) in hours

A: Solid lines —— corange lines (amplitude)($x10^{-9}$)

$$e_{\lambda\theta}(\phi,\lambda,\tau) = A(\phi,\lambda)\cos[\sigma(\tau-\tau_o)-\Delta+\epsilon]$$

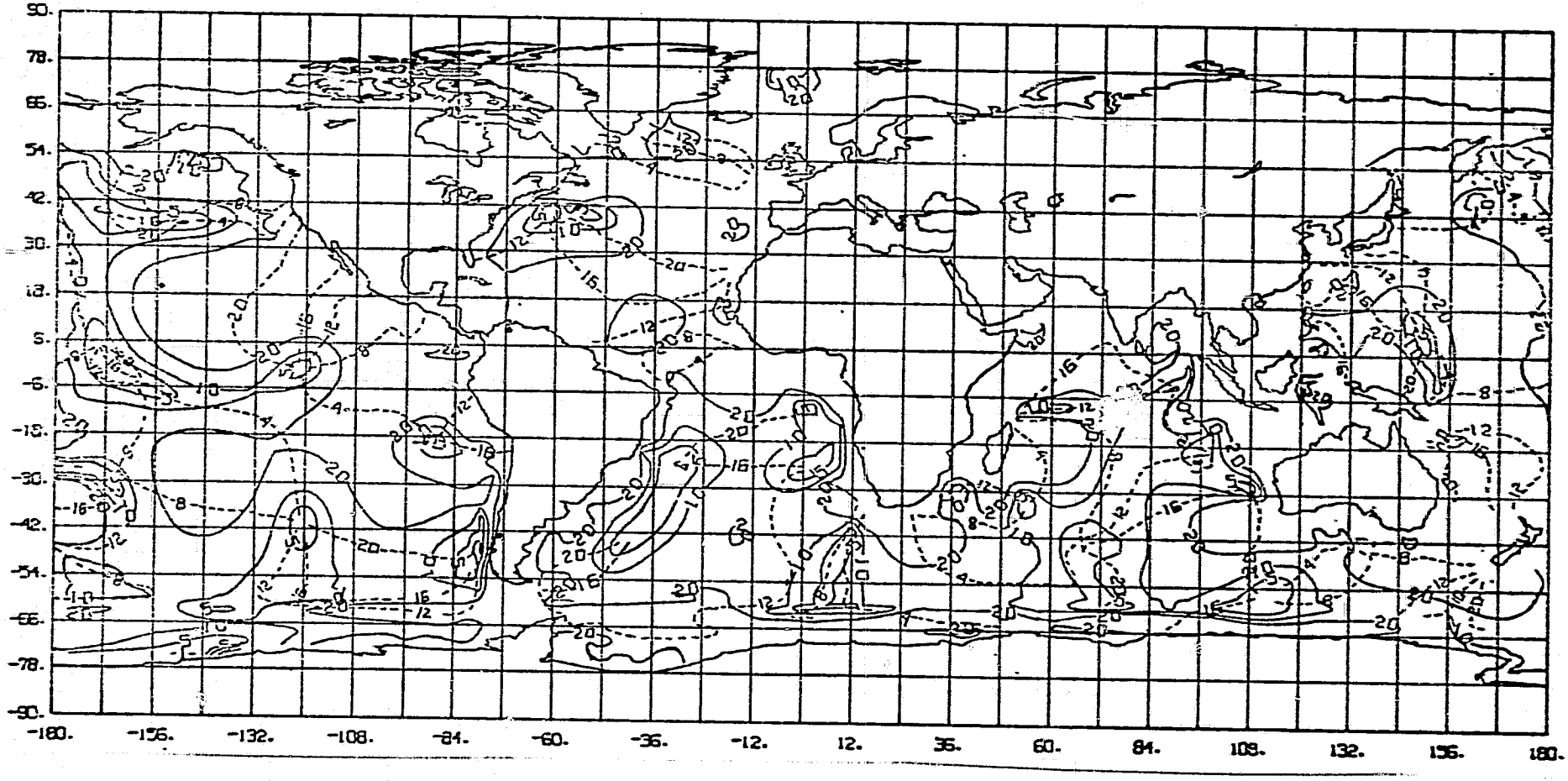

Figure 27

3° x 3° $e_{\lambda\theta}$, Horizontal Surface Strain Component over Land

: Dashed Lines --- cotidal lines (phase) in hours

A: Solid Lines —— corange lines (amplitude)($\times 10^{-10}$)

$$e_{\lambda\theta}(\phi,\lambda;\tau) = A(\phi,\lambda)\cos[\sigma(\tau-\tau_o)-\Delta+\epsilon]$$

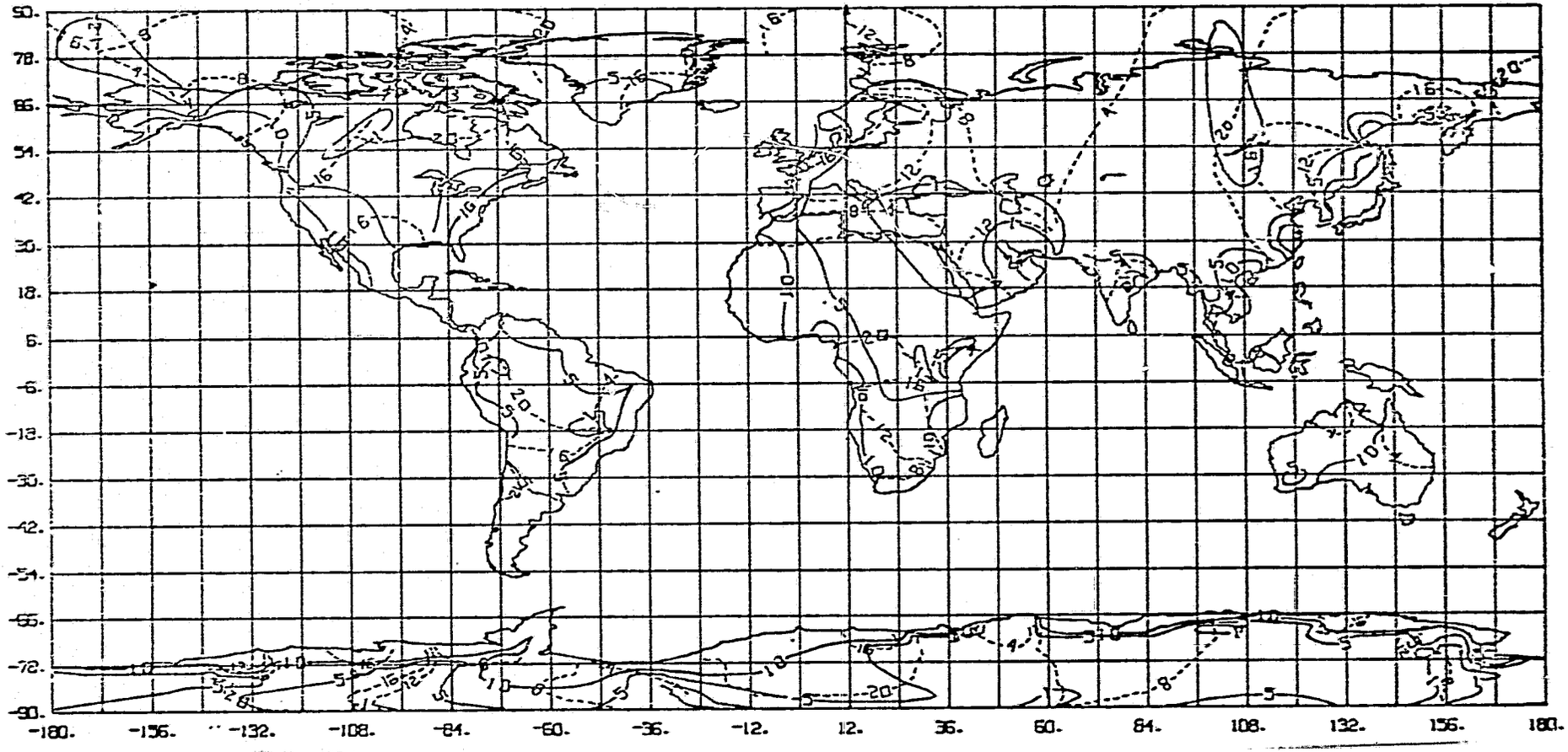

Figure 28

3° x 3° $e_{\lambda\theta}$, Global Horizontal Surface Strain Amplitude

A: Solid Lines —— corange lines (amplitude)($x10^{-10}$)

$$e_{\lambda\theta}(\phi,\lambda;\tau) = A(\phi,\lambda)\cos[\sigma(\tau-\tau_o)-\Delta+\epsilon]$$

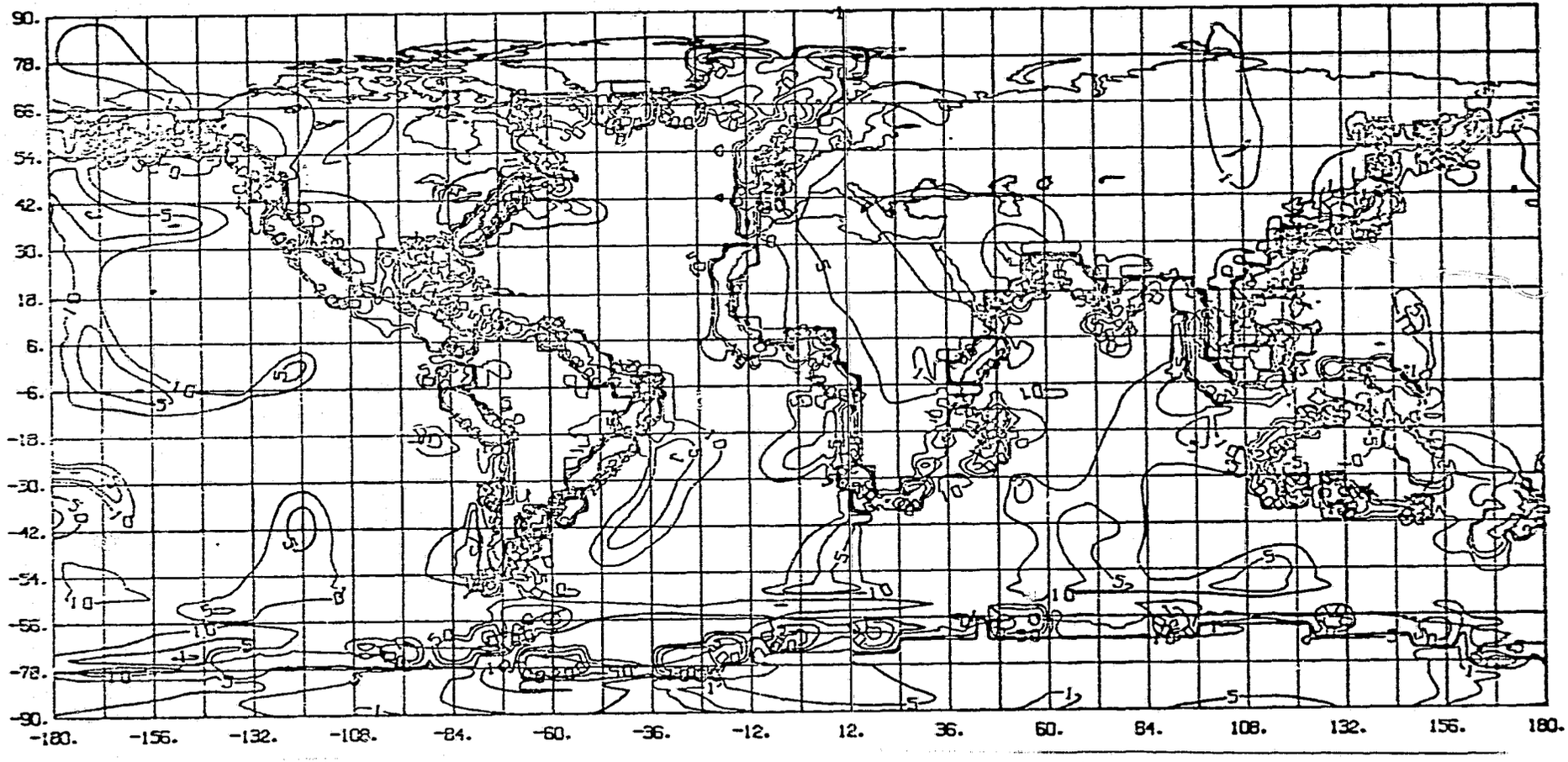

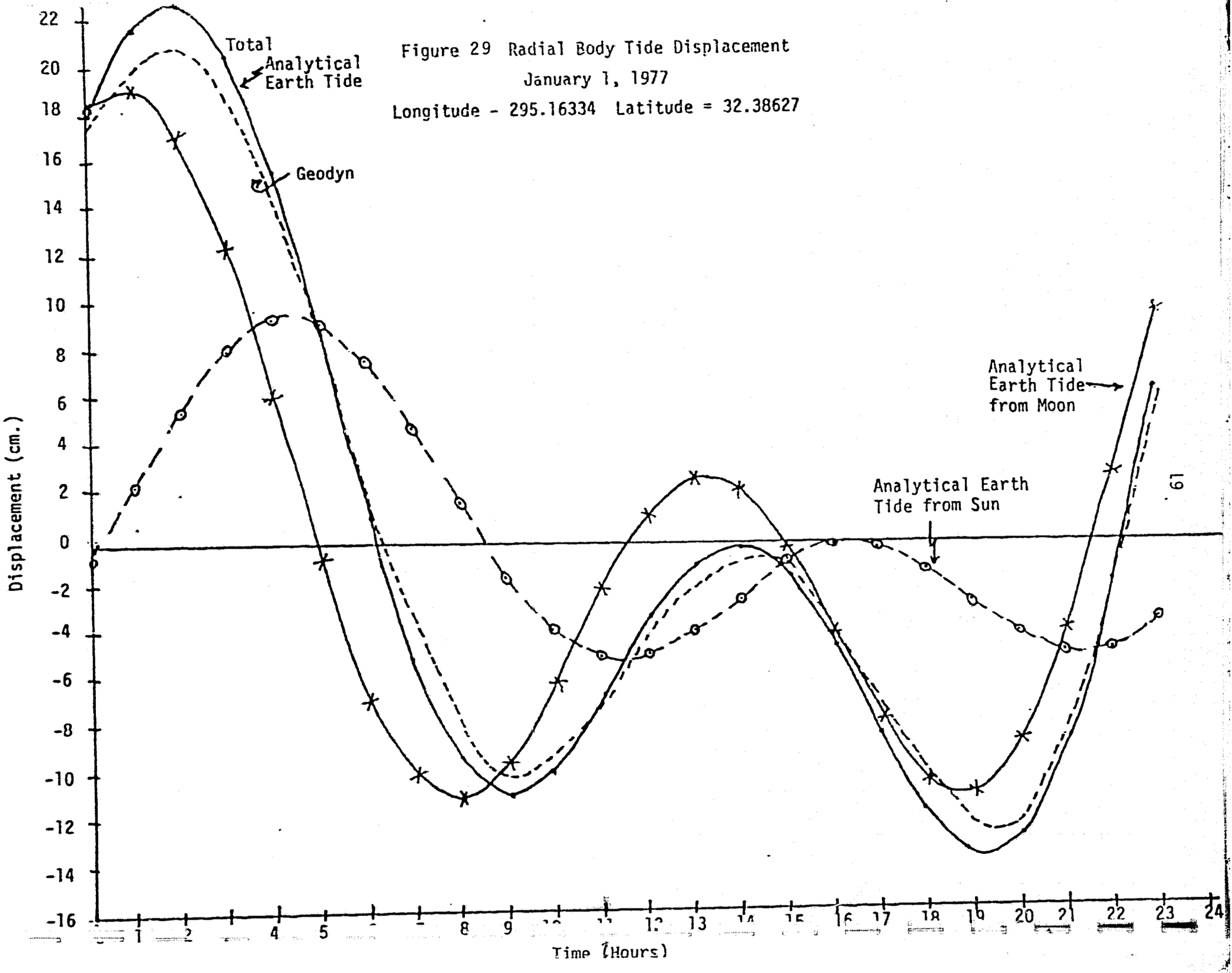

Figure 29 Radial Body Tide Displacement

January 1, 1977

Longitude - 295.16334 Latitude = 32.38627